

# Analysis of the Radiation Balance Components Over Low-turbidity Water Stored in an Agricultural Reservoir in a Tropical Climate

TATYANA KEYTY DE SOUZA BORGES (✉ [tatyana.borges@ifsertao-pe.edu.br](mailto:tatyana.borges@ifsertao-pe.edu.br))

Instituto Federal de Educação Ciência e Tecnologia Goiano: Instituto Federal do Sertão Pernambucano - Campus Ouricuri <https://orcid.org/0000-0002-1700-4150>

AUREO SILVA DE OLIVEIRA

Universidade Federal do Recôncavo da Bahia

RICHARD G. ALLEN

University of Idaho, Idaho, USA

AYSE KILIC

University of Nebraska, Nebraska, USA

JOÃO PAULO CHAVES COUTO

Universidade Federal do Recôncavo da Bahia

CARLOS EDUARDO SANTANA

DANCO Comércio e Indústria de Fumos Ltda.

---

## Research Article

**Keywords:** Radiation Balance Components , Low-turbidity Water Stored, Agricultural Reservoir, Tropical Climate

**Posted Date:** June 1st, 2021

**DOI:** <https://doi.org/10.21203/rs.3.rs-321889/v1>

**License:** © ⓘ This work is licensed under a Creative Commons Attribution 4.0 International License.

[Read Full License](#)

---



## 39 Abstract

40 Understanding how solar and terrestrial radiation fluxes interact with natural surfaces and impact water consumption is of  
 41 wide interest. In eastern sub-humid Bahia, Brazil, scarce surface water stored in lined ponds is used to drip irrigate Sumatra  
 42 tobacco plants grown under partial shading. This work aimed at monitoring, over two irrigation seasons (2015 and 2016),  
 43 the water turbidity, the radiation balance (shortwave – SW and longwave – LW components), and the skin water  
 44 temperature ( $T_w$ ) in the center of a large storage pond to better understand the energy balance of the storage pond and its  
 45 impact on evaporation. Auxiliary data from a collocated weather station were also collected. The water turbidity was very  
 46 low (around 2.6 NTU on average) due to filtration and reverse osmosis of water prior to storage. The mean daily  $T_w$  (26.1  
 47 °C) was nearly always higher than the mean air temperature  $T_a$  (21.8 °C) due to near-surface absorption of solar radiation.  
 48 Incoming ( $S_g$ ) and net SW ( $S_{net}$ ) fluxes decreased by 70% on average with cloud cover while downward LW flux increased  
 49 by 14% due to increased net atmospheric temperature with the presence of clouds. A mean daily albedo of 0.05 was  
 50 measured for the type of water stored in the irrigation tanks. The net LW flux ( $L_{net}$ ) was consistently negative ( $-55.1 \text{ W m}^{-2}$   
 51  $\text{m}^{-2}$  average). Two approaches are proposed for estimating daily net all-wave radiation  $R_n$ . The first is  $R_n = -27.357 +$   
 52  $0.832 \cdot S_{net}$  ( $r^2 = 0.998$  and  $SEE = 9.66 \text{ W m}^{-2}$ ) and the second is  $R_n = S_{net} - L_{net(MLR)}$  where  $S_{net} = 0.95 \cdot S_g$  for both approaches  
 53 and MRL represents a multiple linear regression model ( $r^2 = 0.721$  and  $SEE = 6.87 \text{ W m}^{-2}$ ). Both approaches use data that  
 54 are easily collected from a standard automatic weather station.

55

## 56 1 Introduction

57

58 The surface radiation balance describes the energy converted into sensible and latent heat or into heat storage for a large  
 59 spectrum of processes at the lower boundary of the atmosphere. Its knowledge is of paramount importance in many fields  
 60 of study including hydrology, biology, agriculture, and meteorology. Two radiative properties of a surface (albedo and  
 61 emissivity) dictate the partitioning of shortwave (SW) and longwave (LW) radiation, respectively. Albedo ( $\alpha$ ) characterizes  
 62 the fraction of incoming SW radiation that is reflected back by the surface. Emissivity ( $\epsilon$ ) describes the amount of LW  
 63 radiation that a surface emits relative to a black body at the same temperature (Monteith and Unsworth 2013), according  
 64 to the Stefan-Boltzmann law ( $LW_{emitted} = \epsilon\sigma T^4$ ), where  $\sigma$  is the Stefan-Boltzmann constant ( $5.67 \times 10^{-8} \text{ W m}^{-2} \text{ K}^{-4}$ ) and  $T$  is  
 65 the absolute temperature (K).

66 After reaching the water surface, incoming SW radiation penetrates to a depth that depends on water turbidity  
 67 (transparency) - an optical property that is a function of suspended sediment concentration and dissolved colored materials  
 68 (Marquis 2005). Solar radiation is differentially absorbed according to wavelength ( $\lambda$ ) as it propagates into a water body  
 69 and eventually reaches the bottom of the body if not totally attenuated. In the oceans, according to Wozniak and Dera  
 70 (2007), 94% of the time, downward irradiance is absorbed and converted into other forms of energy below the surface.  
 71 Generally, the infra-red portion of radiation is strongly absorbed in the very thin surface layer while the bluish-green light,  
 72 within the visible portion, penetrates the farthest in optically clear water (Davies-Colley and Smith 2001; Wozniak and  
 73 Dera 2007; Jensen and Allen 2016).

74 The albedo of water surface ( $\alpha_w$ ) varies over the course of a day and during the year because it is a function of solar  
 75 elevation and thus the angle of the direct solar beam to the water surface (Finch and Hall 2005). Adding to this, other  
 76 factors strongly influence  $\alpha_w$  such as the degree of cloudiness that affects the proportion of direct and diffuse radiation,  
 77 water quality, and state of the surface, like height and orientation of waves, which in turn are related to the speed and  
 78 direction of wind over water (Katsaros et al. 1985; Henderson-Sellers 1986; Jin et al. 2004; Finch and Hall 2005; Liu et al.

79 2015). Studies on  $\alpha_w$  have typically been restricted to oceans (Payne 1972; Cogley 1979; Katsaros et al. 1985; Feng et al.  
 80 2016). Over a freshwater lake in Canada, Nunez et al. (1972) reported  $\alpha_w$  varying from 0.07 to 0.11 on a daily basis.  
 81 Typical values for  $\alpha_w$  encompassing variable cloud cover conditions (from clear to overcast skies) are in the range of 0.1-  
 82 0.5 at low sun and 0.03 to 0.1 at high sun (Oke 1995; Shuttleworth 2012). A mean value of  $\alpha_w$  for deep water is in the range  
 83 of 0.04-0.08 (Jensen and Allen 2016).

84 Natural surfaces (soil, vegetation, and water) resemble a black body in the spectral range of terrestrial radiation (3-100  
 85  $\mu\text{m}$ ) with  $\varepsilon$  near 1 according to the Kirchhoff's law, which states that at the same temperature and wavelength good thermal  
 86 absorbers are good thermal emitters (Oke, 1995). For non-black bodies opaque to LW radiation, like water, LW  
 87 transmissivity ( $\tau$ ) is zero and the value of  $\varepsilon$  can be used to approximate the fraction of LW radiation that is reflected back  
 88 to atmosphere, where LW reflectance =  $1 - \varepsilon$  (Oke, 1995). This reflectance is a small fraction, varying from 1% to 10%,  
 89 a reason why many studies assume  $\varepsilon = 1$ , including water surfaces (Finch and Hall 2005). Davies et al. (1971) found water  
 90 emissivity ( $\varepsilon_w$ ) for Lake Ontario to be constant at 0.972 with no apparent influence by changes in the water turbidity and  
 91 chemical composition. In Japan, Konda et al. (1994) considered 0.984 a reliable value for oceanic  $\varepsilon_w$  while Shuttleworth  
 92 (2012) suggested  $\varepsilon_w$  values ranging from 0.92 to 0.97 at small and large zenith angles. Atmospheric emissivity, on the other  
 93 hand, is usually calculated in terms of air temperature, water vapor content and cloud cover (Allen et al., 1998; Bilbao and  
 94 De Miguel 2007; Carmona et al. 2014).

95 Depending on the desired outputs, measurement of  $R_n$  can be made with a single-component, a double-component or  
 96 a four-component net radiometer with the last one providing more detailed information on the radiation balance at the  
 97 surface. Albedo can be derived from measurements made with four-component net radiometers. These are delicate  
 98 instruments that require careful handling. Comparisons among instrument types have been extensive (Field et al. 1992;  
 99 Kustas et al. 1998; Kohsiek et al. 2007; Blonquist et al. 2009). Measurement or estimation of  $R_n$  has been conducted over  
 100 a variety of land-covers including agricultural crops (Sauer et al. 2007; Kohsiek et al. 2007; Ai et al. 2018), natural  
 101 vegetation (Myeni et al. 2020), and wetlands (Vitale et al 2019) as well as lakes and reservoirs (Gianniou and Antonopoulos  
 102 2007; Liu et al. 2015; Aydin and Karakus 2016).

103 Henderson-Sellers (1986) reviewed several methods for calculating  $R_n$  and associated components for modelling lake  
 104 and reservoir evaporation. Incoming and net SW fluxes have been shown to be good estimators of  $R_n$  under both clear and  
 105 cloudy conditions and for a wide range of surfaces, including water (Alados et al. 2003). El Bakry (1993) reported  
 106 regression coefficients for estimation of  $R_n$  using incoming SW radiation at the Aswan High Dam Lake in Egypt and Li  
 107 and Barnes (1980) developed similar relationships for Lake Albert in South Australia. Jensen et al. (1990) made a  
 108 compilation of linear regression coefficients for estimating  $R_n$  for various cropped surfaces.

109 Downing et al. (2006) estimated the global extent of natural lakes in the world to be 4.2 million  $\text{km}^2$  in area for 304  
 110 million water bodies. This large count was dominated by water bodies smaller than 1  $\text{km}^2$ . Water stored in natural lakes  
 111 and impoundments is of great importance for wildlife sustainability, water conservation and crop and animal production.  
 112 Farm ponds have great potential to improve agricultural water security and crop production in many parts of the world  
 113 (Gallego-Elvira et al. 2010). A good example is the cultivation of tobacco in eastern Bahia, Brazil, where this crop is drip-  
 114 irrigated with low-turbidity surface water derived from reverse osmosis and stored in plastic-lined ponds. The reverse  
 115 osmosis is an expensive process that reduces the presence of salts in the irrigation water that degrades the quality of the  
 116 tobacco leaves. The study area is a unique and specialized production system for a high-income crop having an international  
 117 market and is of great importance for the regional economy.

118 Due to the peculiarities of this type of water and considering the tropical characteristics of the region that favor water  
119 loss by evaporation, the objective of this work was to study the time distribution and magnitude of SW and LW components  
120 of the radiation balance as well as surface temperature of stored water from measurements carried out in the center of a  
121 pond. The influence of cloudiness and time of day on all components was studied as well as development of regression  
122 models for predicting radiation fluxes and water albedo in the absence of measurements. This study on radiation balance  
123 is part of a larger study (Borges 2017) on overall surface energy balance for the storage ponds including evaporation.  
124  
125

## 126 **2 Material and methods**

### 127 **2.1 Description of the experimental site**

130 The site was in a private farm owned by a company whose business is to grow, process and export a special type of tobacco  
131 (*Nicotiana tobacco L.*) known as Sumatra. The leaves of this variety are exclusively used for wrapping cigars. The farm is  
132 located in the municipality of Governador Mangabeira, Bahia, Brazil (12° 37' S, 39° 03' W, 218 m asl) where the climate  
133 is a transition between Af (tropical without dry season) and Am (tropical monsoon) climates according to the Köppen  
134 system (Alvares et al. 2013). The mean annual precipitation, air temperature, and relative humidity are around 1100 mm,  
135 25 °C and 75%, respectively. The wind blows mainly from the southeast direction along the year at a 2.5 m s<sup>-1</sup> average  
136 speed.

137 The crop grows under a black nylon mesh for partial shading and is drip-irrigated, as cigar covers burn more uniformly  
138 when chlorine-free water is used for irrigation. Therefore, after being filtered to eliminate solid particles (organic and  
139 inorganic) the naturally abstracted surface water is passed through a reverse osmosis system to remove salts, after which it  
140 is stored in lined reservoirs with a high degree of transparency (low turbidity). The artificial reservoirs are lined with 2-  
141 mm thickness sheets of welded HDPE black plastic. The reservoirs in the farm have trapezoidal cross-sections, with  
142 maximum depth varying from 4 to 8 m and storage capacities ranging from 5,000 to 30,000 m<sup>3</sup>. Currently, about twelve  
143 reservoirs supply water from September to March every season to irrigate, on average, 150 ha of Sumatra tobacco.  
144

### 145 **2.2 Instrumentation and data acquisition**

146  
147 Experimental data were collected over water during the second semesters of 2015 and 2016 using instruments mounted  
148 on-board a handmade floating platform (raft) (FP) (Fig. 1). Details on the design and operation of this platform can be  
149 found in Borges et al. (2016). In 2015, the FP was positioned in the center of the water mirror of a reservoir having  
150 dimensions of 35-m wide (east-west direction) and 85-m long (north-south direction), with 50° average inclination walls,  
151 and with an initial water depth of 5.5 m. Total vertical height from pond bottom to the top of the sides was 6.3 m. In 2016,  
152 the reservoir monitored was deeper with a total vertical height of 8.2 m and 7.5 m of initial water depth). In both cases, the  
153 FP was anchored to the sides of the reservoir by means of nylon ropes.  
154

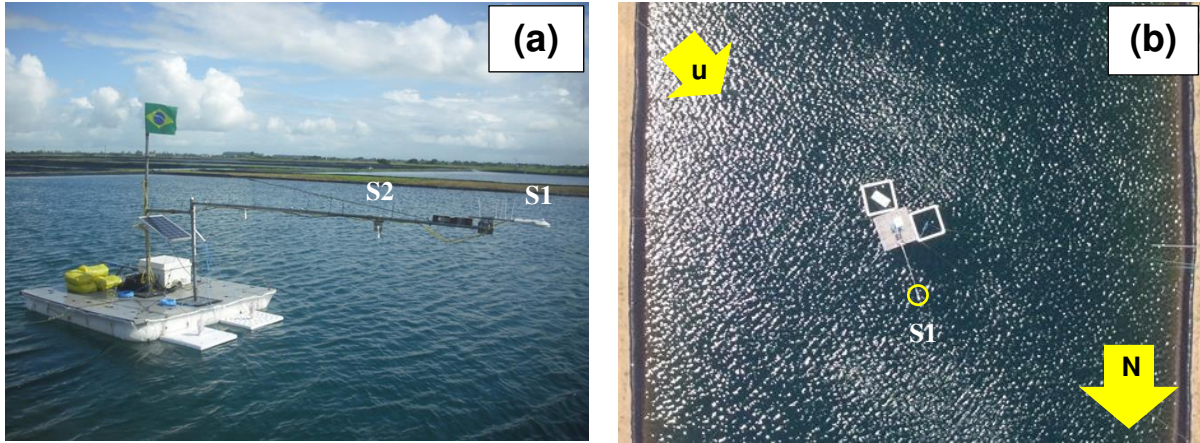


**Fig. 1 a, b** The raft or floating platform (FP) over water with a four-component net radiometer (S1) and an infrared thermometer (S2) in the 2015 and 2016 campaigns. (u = predominant wind direction)

155

156 The radiation balance components at the water surface were measured with a four-component net radiometer (model  
 157 CNR4, Kipp & Zonen). The CNR4 consists of four thermopile sensors with two in the upper face to detect radiation from  
 158 above and the other two in the lower face to detect radiation from the surface. The pyranometers (SW sensors) work in the  
 159 spectral range of 305 to 2,800 nm and the pyrgeometers (LW sensors) in the range of 4,500 to 42,000 nm. Sensors of the  
 160 same type are back facing. The field of view of sensors is 150° in the lower face and 180° in the upper ones. During the  
 161 measurements, the internal temperature of the net radiometer was monitored for correction of detected LW radiation. More  
 162 technical specifications on the CNR4 can be found in documentation by Kipp & Zonen (2010) and Campbell Scientific  
 163 (2014), including the accuracy and fields of view of the sensors. Water turbidity measurements (NTU) were taken with a  
 164 turbidimeter (model OBS3+, Campbell Scientific), positioned at 2 m depth.

165 As shown in Fig. 1b, the CNR4 was positioned 1.15 m above the surface at the end of a 3-m length metal boom  
 166 pointing north. This configuration helped to minimize interference by the raft material on the outgoing radiation detected  
 167 by the sensors. At that height, 99% of the SW and LW radiative fluxes in the underside of the instrument came from a  
 168 footprint area of 415 m<sup>2</sup>, equivalent to a circle having 11.5 m radius, smaller than the minimum distance (17 m) from the  
 169 instrument to the water edge. In the same boom (Fig. 1a), an infrared thermometer (model SI-111, Apogee Instruments)  
 170 was deployed, oriented perpendicular to the surface, for which the footprint area was 0.60 m<sup>2</sup> eliminating, therefore, effects  
 171 of the raft on the sensor signal.

172 The measured outputs of the CNR4 are the incoming SW ( $S_g$ ) and LW ( $L_{atm}$ ) radiation, and the surface-reflected SW  
 173 ( $S_r$ ) and the outgoing LW ( $L_s$ ) radiation. The datalogger output table also included the net SW radiation ( $S_{net} = S_g - S_r$ ) and  
 174 the net LW radiation ( $L_{net} = L_{atm} - L_s$ ) at the surface as well as the surface albedo ( $\alpha = S_r/S_g$ ) and the net all-wave radiation  
 175 ( $R_n = S_{net} - L_{net}$ ).

176 The  $L_s$  component consists of two parallel fluxes: (i) the LW flux emitted by water as a function of its emissivity ( $\epsilon_w$ )  
 177 and absolute temperature according to the Stefan-Boltzmann law (Monteith and Unsworth 2013) and (ii) the incoming LW  
 178 flux reflected by water (Konda et al. 1994). The relationship between them is given by Eq. (1).

179

$$L_e = L_s - L_r \quad (1)$$

180

181 where  $L_e$  is the surface-emitted and  $L_r$  is the surface-reflected LW radiation, both in W m<sup>-2</sup>.

182 In the spectral range of atmospheric emission, the absorptivity of natural surfaces ( $\phi$ ) is equal to its emissivity ( $\epsilon$ )  
 183 (Monteith and Unsworth 2013). For the purpose of this study, we adopted  $\phi_w = \epsilon_w = 0.97$  (Davies et al. 1971), which means  
 184 that  $L_r$  by the low turbidity water surface corresponded to 3% of  $L_{atm}$  according to Eq. (2).  
 185

$$L_r = (L_{atm} - \phi_w L_{atm}) = (1 - \epsilon_w) L_{atm} = 0.03 L_{atm} \quad (2)$$

186  
 187 Additional atmospheric data were obtained with a tripod-mounted weather tower (WT) located in the 2-m wide row  
 188 between tanks and about 10 m from the FP. The rows between tanks in the experimental area are covered with grass and  
 189 are used for the transit of people in the everyday routine of work (tank maintenance, etc.). The tower was equipped with a  
 190 thermo-hygrometer (model HMP60, Vaisala) at 2 m above the ground; an anemometric set for wind direction and speed  
 191 (model 03001, RM Young) at 7 m height in 2015 and 3 m height in 2016; a thermopile pyranometer (model LP02,  
 192 Hukseflux Thermal Systems) in 2015 and a silicon-cell pyranometer (model SPLite, Kipp & Zonen) in 2016, both  
 193 positioned 2.5 m above ground surface. In both seasons, a rain gauge (model TE525MM, Texas Electronics) was used with  
 194 the top cross-section at 0.5 m height. All sensors at the FP and WT were scanned every 30 seconds with a CR1000  
 195 datalogger (Campbell Scientific). Total and mean values were stored at subhourly (5 and 30 min), hourly and daily time  
 196 steps for further analysis.

197 Atmospheric conditions influence the magnitude of the radiation balance components at the surface. Clouds partially  
 198 block the passage of solar radiation and increase atmospheric LW emission (Pashiardis et al. 2017). In this work, the  
 199 atmospheric transmissivity for SW radiation calculated with data from the pyranometers at the WT (Eq. (3)) was used to  
 200 characterize mean daytime cloudiness on a daily basis.  
 201

$$\tau_{atm} = \frac{S_g}{S_o} \quad (3)$$

202  
 203 where  $\tau_{atm}$  is the atmospheric transmissivity for SW radiation (dimensionless) and  $S_o$  is the extraterrestrial solar radiation.  
 204 Calculation of hourly and daily  $S_o$  followed procedures recommended by ASCE (2005).

205 In the absence of clouds (clear sky),  $S_g$  approaches the theoretical maximum  $S_{go}$  which was estimated by Eq. (4)  
 206 (ASCE 2005).  
 207

$$S_{go} = \tau_o S_o = (0.75 + 2 \times 10^{-5} A) S_o \quad (4)$$

208  
 209 where  $S_{go}$  is the incident SW radiation under clear sky conditions,  $\tau_o$  is the estimated atmospheric transmissivity under a  
 210 clear sky (= 0.754) and  $A$  is the local altitude (218 m asl). The  $S_{go}$  calculation was used during quality control and  
 211 assessment of measured  $S_g$  following recommendations of ASCE (2005).

212 Due to the high predominance of days with clouds in both years, the following criterion was used to distinguish the  
 213 degree of average daytime cloudiness over the experimental area:  $\tau_{atm} < 0.20$  (completely cloudy or overcast sky - CCS),  
 214  $0.20 \leq \tau_{atm} < 0.45$  (mostly cloudy sky - MCS),  $0.45 \leq \tau_{atm} < 0.70$  (mostly sunny sky - MSS) and  $\tau_{atm} \geq 0.70$  (completely  
 215 sunny or clear sky - CSS). In spite of being an arbitrary classification, the use of  $\tau_{atm}$  allowed us to define quantitative  
 216 boundaries among the classes of cloud fractions rather than collecting visual observations of sky cover.  
 217

### 218 2.3 Modelling of net radiation fluxes

219

220 In this paper, approaches for modelling net SW radiation ( $S_{net}$ ), net LW radiation ( $L_{net}$ ), and net all-wave radiation ( $R_n$ )  
 221 are tested and evaluated based on daily observation of incoming SW radiation from the net radiometer and air temperature  
 222 and relative humidity measured at the weather tower for both 2015 and 2016 campaigns. Daily data were used because  
 223 models to estimate the components of the radiation balance from atmospheric variables tend to use data commonly obtained  
 224 with standard automatic weather stations and from historical daily weather data sets. Use of readily available data is  
 225 desirable for a wide range of applications. In the tobacco farm, for example, such models can be used to evaluate water  
 226 loss by evaporation from the irrigation tanks, an important type of information for the water management within the  
 227 property.

228 The net SW radiation flux was estimated from incoming SW radiation according to Eq. (5).

229

$$S_{net(e)} = (1 - \alpha_{wc})S_g \quad (5)$$

230

231 where  $S_{net(e)}$  is the estimated daily net SW radiation ( $W m^{-2}$ ) based on a constant value for water surface albedo ( $\alpha_{wc}$ ) and  
 232  $S_g$  is the daily incoming SW radiation from the net radiometer ( $W m^{-2}$ ).

233 Two approaches were considered to model  $L_{net}$ : (i) the same used in the FAO Penman-Monteith equation (Allen et al.,  
 234 1998) to calculate reference evapotranspiration (Eq. (6)) and (ii) a multiple linear regression model (Eq. (7)) having air  
 235 temperature, relative humidity, and an indicator of daytime relative cloudiness as the input variables.

236

$$L_{net(56)} = \sigma \left( \frac{T_x^4 + T_n^4}{2} \right) (0.14 - 0.34\sqrt{e_a}) \left( 1.35 \frac{S_g}{S_{go}} - 0.35 \right) \quad (6)$$

237

238 where  $L_{net(56)}$  is the estimated daily net LW radiation ( $W m^{-2}$ ) according to FAO 56 paper,  $\sigma$  is the Stefan-Boltzmann  
 239 constant ( $5.67 \times 10^{-8} W m^{-2} K^{-4}$ ),  $T_x$  is the daily maximum air temperature (K),  $T_n$  is the daily minimum air temperature  
 240 (K),  $e_a$  is the daily mean actual vapor pressure (kPa),  $S_g$  and  $S_{go}$  are as previously defined. The ratio  $S_g/S_{go}$  represents  
 241 relative cloudiness and in Eq. (6) is limited to  $0.25 < S_g/S_{go} \leq 1.0$  (ASCE, 2005).

242 The multiple linear regression technique (MLR) allows the investigation of an association among three or more  
 243 variables (Akritas 2016) and is generally written as an equation relating the response variable  $Y$  to the predictor variables  
 244  $X_1, \dots, X_k$  and an intrinsic error variable  $\varepsilon$  (Eq. (7)).

245

$$Y = \beta_0 + \beta_1 X_1 + \dots + \beta_k X_k + \varepsilon \quad (7)$$

246

247 where  $\beta_0$  is the intercept and  $\beta_i$  ( $i = 1, 2, \dots, k$ ) are the multiple regression coefficients of the dependent variable  $Y$  (in this  
 248 case  $L_{net(MLR)}$ ) on the independent variable  $X_i$  ( $i = 1, 2, \dots, k$ ).

249 In the present study, atmospheric parameters readily available from weather stations and commonly associated to the  
 250 exchange of LW radiation between the surface and the atmosphere were considered as candidates for independent variables  
 251 in the MLR model. The model was parameterized with data from 2015 using a step-wise procedure in R (R Core Team  
 252 2017) and validated with data collected in 2016. The objective of such a procedure is arriving at an optimal prediction

253 equation by using statistical criteria to eliminate unnecessary predictors leading to the final form of the regression model  
 254 that includes only those predictor variables that can explain the observed variability in the dependent variable.

255 Net all-wave radiation ( $R_n$ ) has been estimated by means of a simple linear regression where  $R_n$  is a function of  
 256 incoming SW radiation or net SW radiation. This method has been widely used over different types of surfaces including  
 257 water (Sene et al. 1991; El Bakry 1993). As the first approach, in this paper  $R_n$  was modelled using  $S_{net(e)}$  as the predictor  
 258 variable (Eq. (8)). The second and third approaches followed the definition of  $R_n$  as the sum of net SW and net LW radiation  
 259 fluxes. Initially,  $R_n$  was given as the sum of Eq. (5) and Eq. (6) and then as the sum of Eq. (5) and Eq. (7).

260

$$R_{n(1)} = a_0 + a_1 S_{net(e)} \quad (8)$$

261

$$R_{n(2)} = S_{net(e)} - L_{net(56)} \quad (9)$$

262

$$R_{n(3)} = S_{net(e)} - L_{net(MLR)} \quad (10)$$

263 where  $R_n$  is the net all-wave radiation ( $W m^{-2}$ ) and  $a_0$  and  $a_1$  are regression coefficients.

264

265

## 266 3 Results and Discussion

267

### 268 3.1 Atmospheric conditions and water turbidity

269

270 Data collected by instruments in the WT from 7<sup>th</sup> Aug. to 29<sup>th</sup> Dec. 2015 (145 days) and from 10<sup>th</sup> Sept. to 31<sup>st</sup> Dec. 2016  
 271 (113 days) were selected to characterize the local atmospheric conditions (Table 1). These time periods represent late winter  
 272 to early summer.

273

274 **Table 1** Summary of daily weather conditions at the experimental site in the 2015 and 2016 campaigns based on  
 275 measurements made at the weather tower

Year	Air temperature (°C)			Relative humidity (%)		Rain depth (mm)	Wind speed (m s <sup>-1</sup> ) <sup>(a)</sup>	Incoming solar radiation (MJ m <sup>-2</sup> day <sup>-1</sup> )		
	Max. <sup>(b)</sup>	Min. <sup>(c)</sup>	Mean	Max.	Min.	Total	Mean	Max.	Min.	Mean
2015	38.1	15.9	24.5	98	32	101	2.7	29.4	7.3	21.7
2016	34.0	19.7	24.9	100	35	146	2.6	27.1	8.3	20.0

276 <sup>(a)</sup> Wind measured at 7 m above ground in 2015 and 3 m above ground in 2016; <sup>(b), (c)</sup> Temperature of the hottest and coldest days

277

278 The atmospheric transmissivity ( $\tau_{atm}$ ) calculated from daily mean values of  $S_g$  (Eq. (3)) ranged from 0.185 to 0.733 in  
 279 2015 and from 0.219 to 0.679 in 2016. In 2015, there was one day with CCS conditions ( $\approx 0.7\%$  of the period), 18 days  
 280 with MCS (12%), 113 days with MSS (68%), and 13 days with CSS (9%). These percentages in 2016 were 0 (no days),  
 281 26% (29 days), 74% (84 days), and 0 (no days), respectively. The predominance of days having cloud cover in the region  
 282 is due to its proximity to the Atlantic Ocean coast (about 60 km to the SE in a straight line), which produces persistent  
 283 cloudiness conditions most of the time.

284 Due to technical problems, the turbidimeter did not work as expected in 2015 but in 2016 water turbidity measurements  
 285 were made continuously for 74 days (18<sup>th</sup> Sept. to 30<sup>th</sup> Nov.). Hourly values of turbidity ranged from 1.7 to 5.4 NTU  
 286 (average of 2.6 NTU), showing an increasing linear trend over time that water was in storage. As mentioned, the low  
 287 turbidity water (high transparency) in the farm reservoirs comes from filtration of organic and mineral fine particles  
 288 followed by reverse osmosis. Therefore, penetration of the blue-green portion of shortwave radiation is expected to be  
 289 relatively deep (Jensen and Allen 2016), and, in the case of the clear ponds with black plastic membranes, most of that  
 290 portion of SW would be absorbed by the black liner.

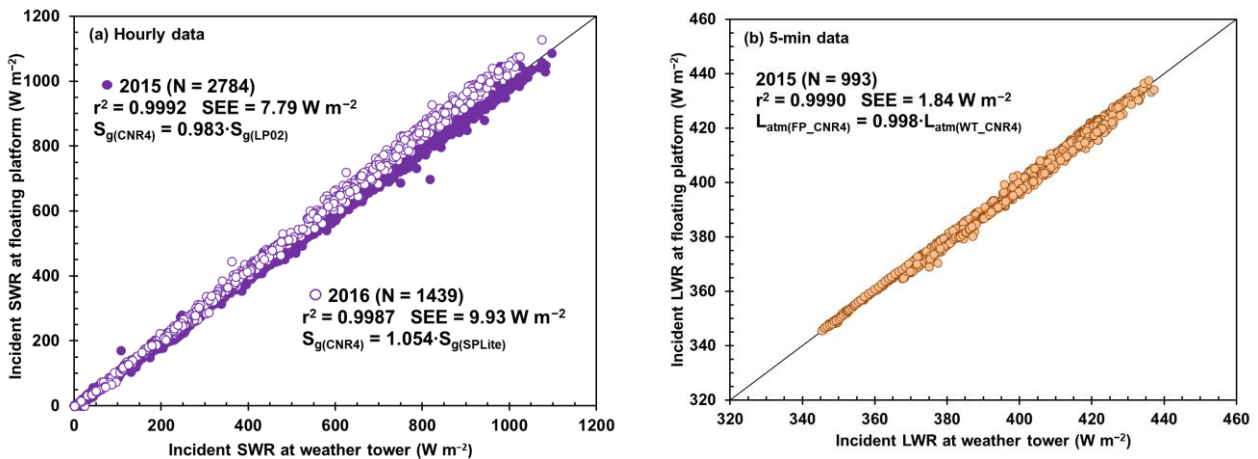
291

### 292 3.2 Incident SW radiation: FP x WT

293

294 As compared to land-based towers, instruments placed on rafts are unstable, oscillating vertically and horizontally due to  
 295 wind effects. Figure 2 compares  $S_g$  and  $L_{atm}$  values measured simultaneously by sensors at the WT and FP. Using the tower  
 296 as reference, the objective was to assess how the instability of the floating device impacted the quality of the readings made  
 297 by the CNR4 over water. As shown in Fig. 2a, the agreement was excellent and visually the distribution of hourly  $S_g$  data  
 298 around the 1:1 line was better in 2015 (number of points,  $N = 2784$ ) when a thermopile pyranometer in the WT was used  
 299 and over water, the CNR4 was just 1.7% lower, on average. In 2016 ( $N = 1439$ ), the agreement between the CNR4 and an  
 300 SPLite pyranometer was also good. It was expected that the LP02 would perform better than the SPLite pyranometer  
 301 (nearer 1 slope and lower SEE), since a silicon-cell based sensor does not measure the full spectrum of solar radiation and  
 302 relies on a single regression correction across distinct cloud conditions. Figure 2b was taken from Borges et al. (2016) who  
 303 compared 5-min  $L_{atm}$  data from two CNR4's in 2015 ( $N = 993$ ).

304



305 **Fig. 2 a, b** Correlation between measurements of SW and LW radiation fluxes from the tripod-mounted weather tower  
 306 and the floating platform. SW radiation was measured with pyranometers in the tower and with the CNR4 net radiometer  
 307 in the floating platform while LW radiation was measured with two CNR4's. Data of (b) are from Borges et al. (2016)

308

309 The good correlation (high  $r^2$  and low SEE) of linear regressions through origin shown in Fig. 2 for both SW and LW  
 310 fluxes suggests that measurements over water were not negatively impacted by FP oscillation and that the CNR4 data  
 311 collected in this two-year study are of good quality. Although vertical oscillations alter the leveling of the instrument, on  
 309 average the impacts of the oscillations tended to cancel out even for averages taken over short periods (hourly for SW and  
 310 5-min interval for LW radiation).

311

### 312 3.3 Seasonal analysis of radiation balance components

313

314 The period of measurements with the FP in 2015 covered 175 days (from 11<sup>th</sup> Jun. to 2<sup>nd</sup> Dec.) but in 2016 this interval  
 315 was shorter (74 days, from 18<sup>th</sup> Sept. to 30<sup>th</sup> Nov.), due to technical problems that delayed sensor deployment. Unlike 2016,  
 316 failures in data collection occurred in 2015, especially in the first half of the period. Thus, the 74-day period of 2016 in  
 317 common with 2015 was used for comparison purposes. Table 2 summarizes daily mean values for all components of the  
 318 radiation balance. To facilitate comparisons, all fluxes are shown as positive. It is common, however, to consider radiative  
 319 fluxes oriented toward the surface as positive and as negative those in the opposite direction (Shuttleworth 2012). In  
 320 general, the values were quite similar between both years.

321

322 **Table 2** Values for mean and amplitude (range) of the 24-hour radiation balance components at the low-turbidity water  
 323 surface in 2015 and 2016 campaigns from 18<sup>th</sup> Sept. to 30<sup>th</sup> Nov.

Year	Statistics	Radiation flux density ( $\text{W m}^{-2}$ )							
		$S_g$	$S_r$	$S_{\text{net}}$	$L_{\text{atm}}$	$L_r$	$L_e$	$L_{\text{net}}$	$R_n$
2015	Mean	249.9	11.5	238.4	398.8	11.9	443.3	56.7	181.7
	(Range)	(83-321)	(5-14)	(78-308)	(374-429)	(11-13)	(431-458)	(33-76)	(41-244)
2016	Mean	241.7	9.1	232.6	402.4	12.0	443.8	53.5	179.2
	(Range)	(101-328)	(5-11)	(95-317)	(368-433)	(11-13)	(434-451)	(26-81)	(64-252)
Both	Mean	245.8	10.3	235.5	400.6	11.9	443.5	55.1	180.4

324  $S_g$  = incoming SW radiation;  $S_r$  = reflected SW radiation;  $S_{\text{net}}$  = net SW radiation;  $L_{\text{atm}}$  = incoming LW radiation;  $L_r$  =  
 325 reflected LW radiation;  $L_e$  = emitted LW radiation;  $L_{\text{net}}$  = net LW radiation, and  $R_n$  = net all-wave radiation

326

327

328 Figure 3, showing data from the 2016 campaign only, illustrates the time variation of the radiation balance components.  
 329 Incoming fluxes were plotted as positive and outgoing ones as negative. In order to better visualize variations in the  $S_r$  and  
 330  $L_r$  curves, the values were multiplied by a factor of 10. In this paper, daily water surface albedo ( $\alpha_w$ ), as shown in Fig. 3b,  
 331 was calculated as the ratio of 24-h mean values of  $S_r$  to  $S_g$ . In 2015, the daily  $\alpha_w$  varied from 0.034 to 0.072 with an average  
 332 of 0.050 and in 2016 it varied from 0.031 to 0.067 with an average value of 0.044. Considering both years, the daily mean  
 333  $\alpha_w$  was 0.047. Albedo generally increased to above 0.06 on cloudy days as evidenced by low  $S_{\text{net}}$  and generally decreased  
 334 to near 0.04 on relatively clear days. These results are consistent with Jensen and Allen (2016) who highlighted the low  
 335 average value of water albedo (0.06) compared to other surfaces, like vegetation. In agricultural crops, for example, the  
 336 mean albedo varies from 0.20 to 0.25. Henderson-Sellers (1986) and Shuttleworth (2012) suggest a mean albedo of 0.08  
 337 for water with the effects of cloud cover included.

338

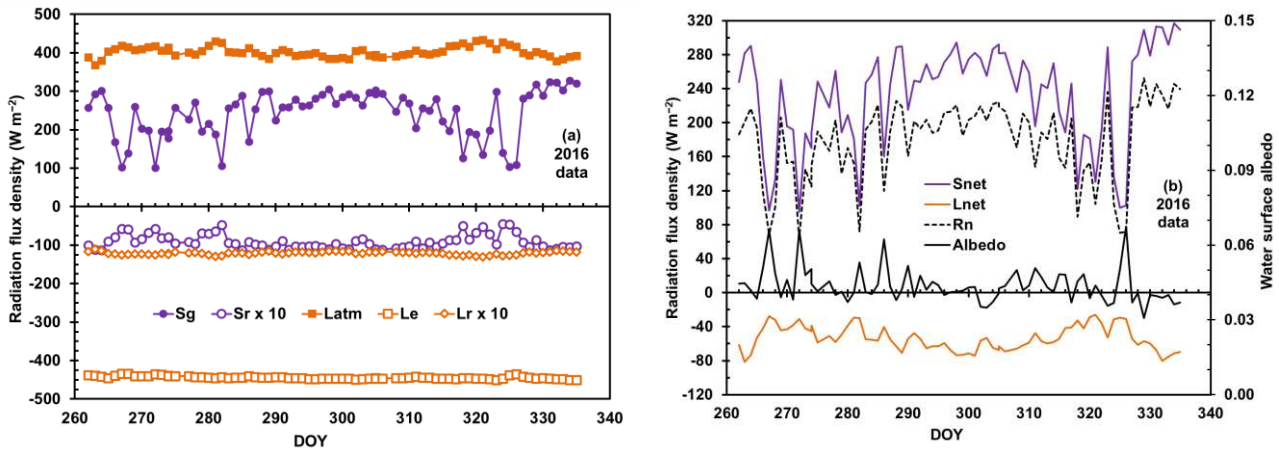


**Fig. 3 a, b** Seasonal variation of daily components of the radiation balance over the surface of the low-turbidity water from 18<sup>th</sup> Sept. (DOY 262) to 30<sup>th</sup> Nov. 2016 (DOY 335)

339

340 For the entire period, absolute  $L_e$  was greater in magnitude than  $L_{atm}$  and, therefore,  $L_{net}$  (Fig. 3b) was consistently  
 341 negative with a  $53.5 \text{ W m}^{-2}$  daily average (Table 2). This indicates that the surface loses more long-wave radiation than it  
 342 gains from the atmosphere. Figure 3a shows that the  $L_{atm}$  data series had greater variability ( $13.7 \text{ W m}^{-2}$  std. dev.) than did  
 343  $L_e$  ( $3.7 \text{ W m}^{-2}$  std. dev.), reflecting impacts of changes in cloud cover that govern atmospheric emission as well as effects  
 344 of air temperature oscillations relative to water temperature. In 2016, the mean temperature of water surface ( $27.3 \text{ }^\circ\text{C}$ ) was  
 345 higher than that of air ( $24.9 \text{ }^\circ\text{C}$ ) and varied from  $26.0 \text{ }^\circ\text{C}$  to  $28.2 \text{ }^\circ\text{C}$  while for the air it varied from  $21.8 \text{ }^\circ\text{C}$  to  $27.2 \text{ }^\circ\text{C}$ .

346 Cloudiness caused variability in  $S_g$  and  $S_{net}$  as well as in  $R_n$  that was the most pronounced among all components as  
 347 shown in Fig. 3. As previously mentioned, there were no completely clear sky days over the area in 2016. While  $S_{net}$  was  
 348 always positive over time,  $L_{net}$  was always negative, which typically occurs over natural surfaces. The daily net all-wave  
 349 radiation  $R_n$  was always positive ( $S_{net} > L_{net}$ ), with negative values observed during nighttime and positive ones during  
 350 daytime. The  $S_{net}$  and  $R_n$  curves followed the  $S_g$  variation closely and, on average,  $R_n$  corresponded to 74% of  $S_g$  (77% of  
 351  $S_{net}$ ), evidencing the smaller contribution of the net LW balance ( $L_{net}$ ) to  $R_n$ .

352

353

### 354 3.4 Effects of cloud cover

355

#### 356 3.4.1 SW and LW radiation fluxes

357

358 Two days from each year with contrasting atmospheric transmissivity ( $\tau_{atm}$ ) were selected to contrast the effects of cloud  
 359 cover on the radiation balance for the low-turbidity water surface. Table 3 summarizes, in decreasing order of  $\tau_{atm}$ , the  
 360 statistics for the selected days, namely, 4<sup>th</sup> Sept. 2015 (DOY 247), 5<sup>th</sup> Nov. 2016 (DOY 310), 12<sup>th</sup> Oct. 2016 (DOY 286),  
 361 and 30<sup>th</sup> Oct. 2015 (DOY 303). For these days,  $\tau_{atm}$  was 0.72, 0.55, 0.36, and 0.18, respectively.

362 As expected, short-wave radiation components were strongly affected by the presence of clouds. From CSS  
 363 (completely sunny sky,  $\tau_{atm} = 0.72$ ) to CCS conditions (completely cloudy sky,  $\tau_{atm} = 0.18$ ),  $S_g$  varied from  $278.1 \text{ W m}^{-2}$   
 364 to  $83.4 \text{ W m}^{-2}$ , a 70% reduction. Similar percent reductions in  $S_r$  and  $S_{net}$  were also observed, as shown in Table 3.

365

366

367 **Table 3** Mean absolute values of the radiation balance components measured over a low-turbidity water surface during the  
 368 2015 and 2016 campaigns using four selected example days having contrasting daytime cloud cover

Radiation flux density ( $\text{W m}^{-2}$ )	CSS ( $\tau_{\text{atm}} = 0.72$ ) DOY 247/2015	MSS ( $\tau_{\text{atm}} = 0.55$ ) DOY 310/2016	MCS ( $\tau_{\text{atm}} = 0.36$ ) DOY 286/2016	CCS ( $\tau_{\text{atm}} = 0.18$ ) DOY 303/2015
$S_g$	278.1	268.9	169.1	83.4
$S_r$	12.6	10.2	9.1	5.1
$S_{\text{net}}$	265.6	258.7	160.1	78.3
$L_{\text{atm}}$	364.1	397.8	411.7	415.2
$L_r$	10.9	11.9	12.3	12.5
$L_e$	434.4	444.4	439.9	440.3
$L_{\text{net}}$	81.2	58.5	40.5	37.5
$R_n$	184.3	200.2	119.6	40.8

369 CSS = completely sunny (clear) sky; MSS = mostly sunny sky; MCS = mostly cloudy sky; CCS = completely cloudy (overcast) sky

370

371 The atmospheric emission of LW radiation ( $L_{\text{atm}}$ ) showed an increasing trend with cloud cover from  $364.1 \text{ W m}^{-2}$  to  
 372  $415.2 \text{ W m}^{-2}$ , a 14% variation. The presence of clouds increases atmospheric emissivity ( $\epsilon_{\text{atm}}$ ) due to generally lower  
 373 altitudes of clouds compared to the net altitude of emitting clear air columns (Bilbao and De Miguel 2007; Carmona et al.  
 374 2014). LW emission is also higher from clouds due to their generally higher temperature compared to an emitting clear air  
 375 column. This is governed by the emission of LW radiation being proportional to its emissivity and the fourth power of its  
 376 absolute temperature according to Stefan-Boltzmann's law (Monteith and Unsworth 2013). The LW radiation emitted by  
 377 the low-turbidity water surface ( $L_e$ ) showed no trend and differences among the four days were small ( $11 \text{ W m}^{-2}$  range)  
 378 due to the relatively constant water surface temperature observed in all days. Both  $L_e$  and  $L_{\text{net}}$  were influenced by water  
 379 surface temperature, which in turn depends, among many factors, on the aerodynamic conditions at the surface-atmosphere  
 380 interface, as wind speed which generates turbulence and mixing. The LW radiation reflected by water,  $L_r$ , followed the  
 381 same trend as for  $L_{\text{atm}}$ , since the earlier was set as a constant fraction of the latter. The behavior of outgoing LW radiation  
 382 ( $L_r + L_e$ ) showed no trend with cloud cover relative to the behavior of  $L_{\text{atm}}$ . This resulted in  $L_{\text{net}}$  also decreasing with the  
 383 degree of cloudiness, a reduction of about 54%.

384 Since  $S_g$  is the main input for the net all-wave radiation  $R_n$ , higher values of  $R_n$  at water surface were observed under  
 385 higher  $\tau_{\text{atm}}$  indicating impacts of higher availability of shortwave energy under clear or near clear sky conditions that were  
 386 greater than reductions in  $L_{\text{atm}}$ , on average. A large fraction of this energy is transmitted and absorbed within the water  
 387 body before eventually reaching the bottom of the reservoir. On the other hand,  $R_n$  increased from DOY 247 ( $\tau_{\text{atm}} = 0.72$ )  
 388 to DOY 310 ( $\tau_{\text{atm}} = 0.55$ ) because while reduction in  $S_g$  was only  $9.2 \text{ W m}^{-2}$ , the increase in the LW input ( $L_{\text{atm}}$ ) was almost  
 389 four times more ( $33.7 \text{ W m}^{-2}$ ) due to the effects of relatively warm clouds. As can be seen from Table 3, on a daily basis,  
 390 LW fluxes were higher than SW fluxes, especially under cloudy conditions, indicating the importance of LW measurement  
 391 or estimation in  $R_n$  calculations. However, the net contribution of SW components to  $R_n$  is more relevant since opposite  
 392 fluxes of LW radiation (downward  $L_{\text{atm}}$  and upward  $L_e$ ) tend to offset each other (Campbell and Norman 1998; Jensen and  
 393 Allen 2016) as observed by Gianniou and Antonopoulos (2007) over Lake Vegoritis in Greece and by many others.

394 Figure 4 illustrates the time distribution of the radiation balance components for the four days in Table 3, including  
 395 the envelope of clear-sky solar radiation  $S_{g0}$  for reference (Eq. (4)). As in Fig. 3, values for  $S_r$  and  $L_r$  were multiplied by 10  
 396 to better illustrate variations. As expected, the reduction in  $S_g$  compared to  $S_{g0}$  increased as the cloud cover increased. On  
 397 DOY 247 the reduction was just 7% (from  $S_{g0} = 299.3 \text{ W m}^{-2}$  to  $S_g = 278.1 \text{ W m}^{-2}$ ) followed by 22% on DOY 310, 50%  
 398 on DOY 286, and finally 76% reduction on DOY 303 when the sky was covered by dense clouds all day. On this particular

399 day (303),  $S_g$  (average  $83.4 \text{ W m}^{-2}$ ) was much smaller than the maximum expected  $S_{g0}$  (average  $343.2 \text{ W m}^{-2}$ ). In all days,  
 400  $R_n$  followed  $S_g$  very closely, regardless of the degree of cloud cover, with  $R_n$  experiencing a reduction of about 78% from  
 401 the clear sky to the overcast sky (Table 3). On the day with the highest atmospheric transmissivity (DOY 247),  $S_g$  peaked  
 402 above  $S_{g0}$  envelope at around 1100 h probably due to nearby clouds that reflected additional shortwave radiation upon the  
 403 pyranometer (Allen 1996).  
 404

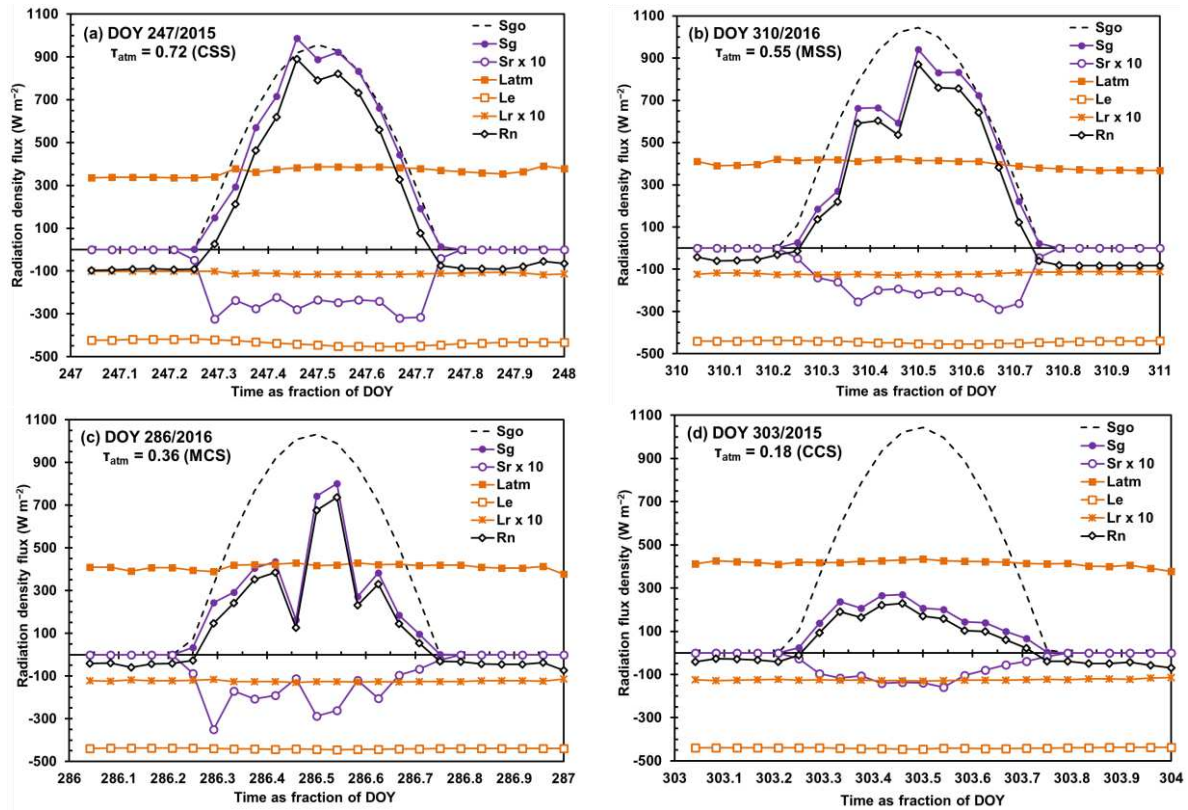


**Fig. 4 a, b, c, d** Daily course of radiation balance components on the surface of low turbidity water as a function of cloud cover expressed by  $\tau_{atm}$  (the daytime atmospheric transmissivity) for the four selected days from 2015 and 2016. CSS = completely sunny (clear) sky, MSS = mostly sunny sky, MCS = mostly cloudy sky, and CCS = completely cloudy (overcast) sky

405

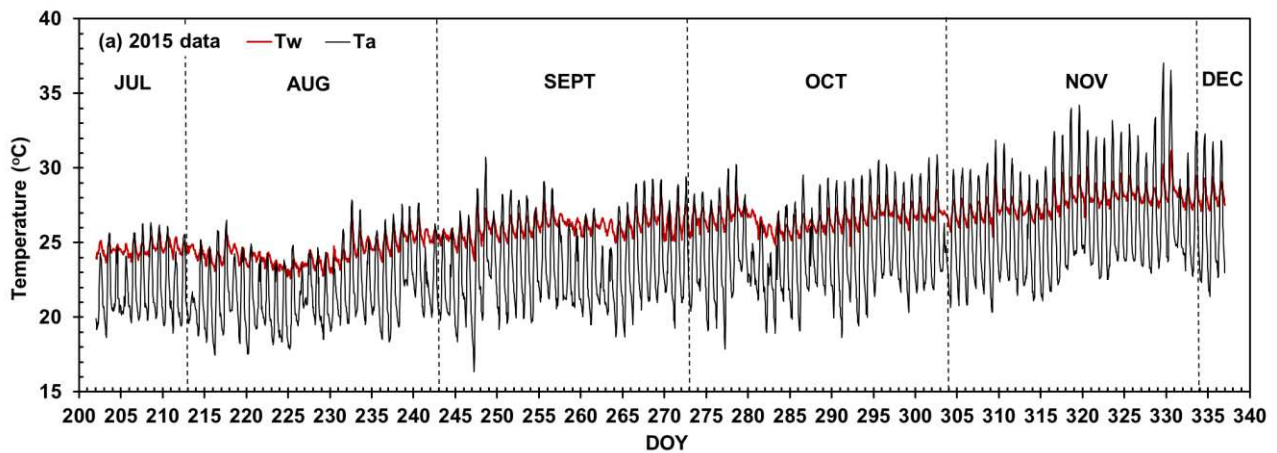
406 Figure 4 also shows that the degree of cloudiness affected not only the amount of solar radiation reflected by the water  
 407 surface (a daily average reduction of 59% (Table 3) from clear to overcast sky) but the shape of the  $S_r$  curve. On DOY 247  
 408 (clear sky), the maximum values for  $S_r$  were concentrated on times of the day having low sun angle (early in the morning  
 409 and late afternoon) while it was relatively constant in between. The opposite was observed on DOY 303 (overcast sky),  
 410 when  $S_r$  peaked around noon with the minimum values at times of low sun angles. Under such conditions,  $S_r$  was less early  
 411 in the morning and late afternoon compared to DOY 247 since clouds blocked solar radiation reducing  $S_g$ . The  $S_r$  peaked  
 412 around noon on DOY 303 because under high cloudiness it is expected that diffuse radiation coming from all angles of the  
 413 hemispherical sky (Katsaros et al. 1985) reaches the surface in higher proportion compared to the direct beam, with low  
 414 angles of incidence having higher albedo.

415

416 Within a day, the LW emission by atmosphere and water surface did not express extensive variation over the course  
 417 of 24 hours. However, comparing the two cases of extreme daytime atmospheric transmissivity (Fig. 4a and 4d),  $L_{atm}$  and  
 418  $L_e$  showed an opposite behavior in terms of amplitude. On DOY 247 ( $\tau_{atm} = 0.72$ ), the range of  $L_{atm}$  ( $54 \text{ W m}^{-2}$ , min =  $336$   
 $\text{W m}^{-2}$  and max =  $390 \text{ W m}^{-2}$ ) was slightly lower compared to DOY 303 ( $\tau_{atm} = 0.18$ ) with a range of  $57 \text{ W m}^{-2}$  (min =

419  $378 \text{ W m}^{-2}$  and  $\text{max} = 435 \text{ W m}^{-2}$ ) but  $L_e$  ranged much more ( $36 \text{ W m}^{-2}$ ,  $\text{max} = 454 \text{ W m}^{-2}$  and  $\text{min} = 418 \text{ W m}^{-2}$ ) on DOY  
 420 247 relative to DOY 303 ( $8 \text{ W m}^{-2}$ ,  $\text{max} = 444 \text{ W m}^{-2}$  and  $\text{min} = 436 \text{ W m}^{-2}$ ). In general, in all four days both atmosphere  
 421 and water LW emission varied less over 24-hour periods as cloud cover increased. The daily amplitude in  $R_n$  decreased  
 422 with cloud cover. On DOY 247,  $R_n$  varied from  $889 \text{ W m}^{-2}$  to  $-98 \text{ W m}^{-2}$  and from  $228 \text{ W m}^{-2}$  to  $-70 \text{ W m}^{-2}$  on DOY 303.  
 423 The average nighttime values for  $R_n$  were  $-46 \text{ W m}^{-2}$ ,  $-34 \text{ W m}^{-2}$ ,  $-23 \text{ W m}^{-2}$ , and  $-22 \text{ W m}^{-2}$  on DOY's 247, 310, 286,  
 424 and 303, respectively. Larger ranges for  $L_e$  observed on a clear day compared to a cloudy day is because during daytime  
 425 on a clear day, the upper water layer is heated more intensively by solar radiation which increases its temperature and  
 426 radiation emission. During nighttime it loses more radiation as LW emission, therefore decreasing its temperature.

427 Figure 5 summarizes an analysis of seasonal and daily courses for water and air temperatures (respectively,  $T_w$  and  
 428  $T_a$ ). Fig. 5a shows how hourly data for  $T_w$  and  $T_a$  varied within each day from the 21<sup>st</sup> July (DOY 202) to 2<sup>nd</sup> Dec. (DOY  
 429 336) in 2015, encompassing most parts of winter and spring in the southern hemisphere.  $T_w$  was measured with the infrared  
 430 thermometer depicted in Fig. 1 and  $T_a$  was measured at 2 m height in the weather tower nearby the water tank where the  
 431 FP was deployed. It can be seen from Fig. 5a that  $T_a$  was consistently below  $T_w$  except during afternoon when  $T_a$  peaked  
 432 above  $T_w$  for most days, mainly from mid-October. Some of the elevation of  $T_a$  over  $T_w$  was caused by heating of surface  
 433 air by land surfaces upwind of the ponds during afternoon and by evaporative cooling of the pond surfaces. During periods  
 434 of low SW,  $T_a$  was typically well below that of the more constant  $T_w$ . Additionally, for all days during the period, the daily  
 435 amplitude in  $T_a$  ( $\Delta T_a$ ) was substantially higher than that for  $T_w$  ( $\Delta T_w$ ) due to the large amount of heat capacitance of the  
 436 water. The resistance of water in changing temperature is due to its higher heat capacity ( $4180 \text{ kJ m}^{-3} \text{ K}^{-1}$ ) and depth as  
 437 compared to air ( $1.2 \text{ kJ m}^{-3} \text{ K}^{-1}$ ) at  $25 \text{ }^\circ\text{C}$ . On average, both  $T_w$  and  $T_a$  tended to increase over time as the days passed from  
 438 winter to spring, reflecting the availability of energy at the surface. Based on daily mean values,  $T_w$  was higher than  $T_a$ ,  
 439 except on three days (DOY 214, 216, and 241) when  $T_w$  was slightly lower probably due to colder air masses entering the  
 440 region which is common in winter. The daily difference between  $T_w$  and  $T_a$  varied from  $-0.2 \text{ }^\circ\text{C}$  to  $8.6 \text{ }^\circ\text{C}$ . For the entire  
 441 2015 season (Fig. 5a), daily mean  $T_w$  was  $26.1 \text{ }^\circ\text{C}$  ( $\text{max} = 29.0 \text{ }^\circ\text{C}$ ,  $\text{min} = 23.3 \text{ }^\circ\text{C}$ ) compared to daily mean  $T_a$  on the order  
 442 of  $21.8 \text{ }^\circ\text{C}$  ( $\text{max} = 26.3 \text{ }^\circ\text{C}$ ,  $\text{min} = 18.7 \text{ }^\circ\text{C}$ ). These outcomes illustrate the strong influence of warming of the water surface  
 443 by near-surface absorption of infrared and near-infrared radiation (Jensen and Allen 2016) relative to the overlying air.  
 444



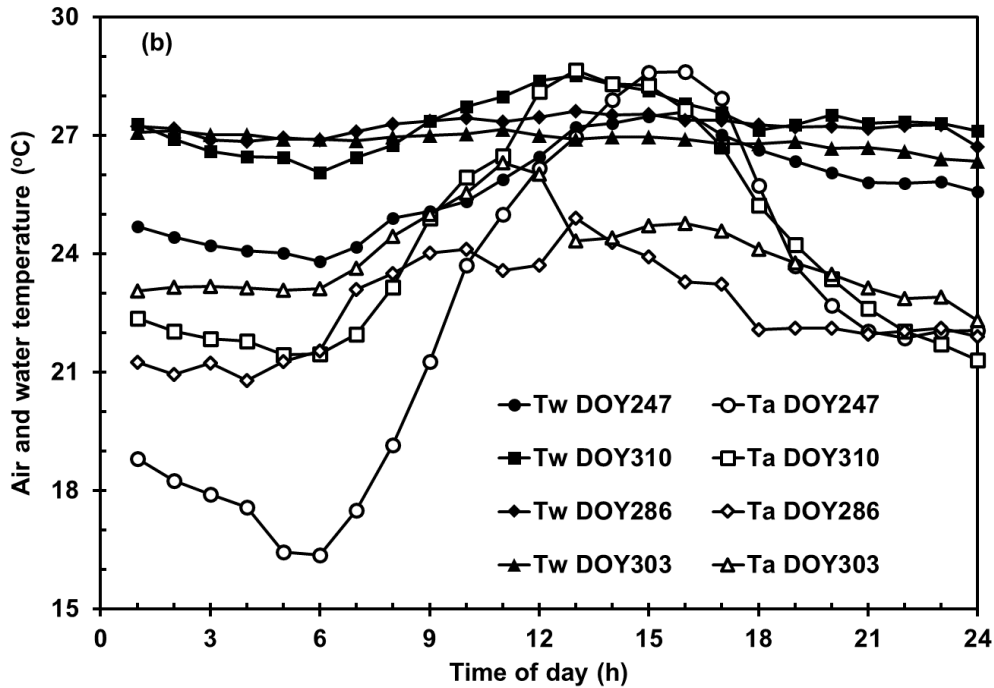


**Fig. 5 a, b** Time trends in water surface ( $T_w$ ) and air ( $T_a$ ) temperatures from mid-July to early December 2015 and  $T_w$  and air temperature  $T_a$  for the selected days with contrasting cloud cover. DOY 247/2015 (CSS,  $\tau_{\text{atm}} = 0.72$ ), DOY 310/2016 (MSS,  $\tau_{\text{atm}} = 0.55$ ), DOY 286/2016 (MCS,  $\tau_{\text{atm}} = 0.36$ ), and DOY 303/2015 (CCS,  $\tau_{\text{atm}} = 0.18$ ). CSS = completely sunny (clear) sky, MSS = mostly sunny sky, MCS = mostly cloudy sky, and CCS = completely cloudy (overcast) sky

445

446

447

448

449

450

451

452

453

454

455

456

457

458

459

460

461

462

463

464

465

The impact of cloud cover on daily variation of  $T_w$  and  $T_a$  is shown in more detail in Fig. 5b for the four selected days from Table 3 with contrasting  $\tau_{\text{atm}}$ . As already shown in Fig. 5a, in general,  $T_w$  was higher than  $T_a$  most of the time regardless the cloud cover, especially during nighttime. Daily mean temperatures for water and air did not follow any noticeable trend with cloud cover, which suggests that average temperature near or at the water surface cannot be solely explained based on degree of cloudiness. However, this is not the case for daily range in temperature ( $\Delta T$ ) as can be deduced from Fig. 5b, because for both water and air,  $\Delta T$  decreased as cloud cover increased.  $\Delta T_w$  varied from 3.8 °C (DOY 247,  $\tau_{\text{atm}} = 0.72$ ) to 0.8 °C (DOY 303,  $\tau_{\text{atm}} = 0.18$ ) and  $\Delta T_a$  varied from 12.3 °C (DOY 247) to 4.0 °C (DOY 303). In fact,  $T_w$  virtually did not change over time on DOY 286 and 303, the two days having the highest cloud cover. This was due to the reduction in shortwave energy during daytime and consequent warming of water, as well as moderation of effective sky temperature by clouds. This atmospheric condition affected  $T_a$  as well, since those days had the lowest  $\Delta T_a$ . The presence of clouds seems to make the pattern in temperature variation over time unclear for both  $T_w$  and  $T_a$ , which means that the moments of occurrence of daily maximum and minimum temperatures cannot be precisely predicted as for clear or nearly clear sky days.

### 3.4.2 Albedo of the water surface

Figure 6 shows the daily course of water albedo ( $\alpha_w$ ) for the four selected days. In Fig. 6a,  $\alpha_w$  is given as a function of sun elevation angle ( $\theta$ ) in the range of 0 to 90° using 5-min data, while in Fig. 6b, hourly values were used to plot albedo as a function of local time. Clearly,  $\alpha_w$  tended to decrease as  $\theta$  increased which agrees with other studies (Katsaros et al. 1985; Jin et al. 2004). Most of the albedo plotted in Fig. 6a are below 0.30. However, high values for albedo (> 0.50)

466 occurred with low  $\theta$  at sunrise and sunset (Fig. 6a) regardless of cloud cover conditions. It is difficult to interpret albedo  
 467 values occurring early in the morning and late afternoon. It is known that, physically, sun glint is a phenomenon that causes  
 468 the very high values of  $\alpha_w$  at these times under clear sky conditions. It is also possible that albedo was impacted, to some  
 469 degree, by sensor oscillation in the floating platform (Fig. 1) and sides of the water reservoir at low  $\theta$ .  
 470

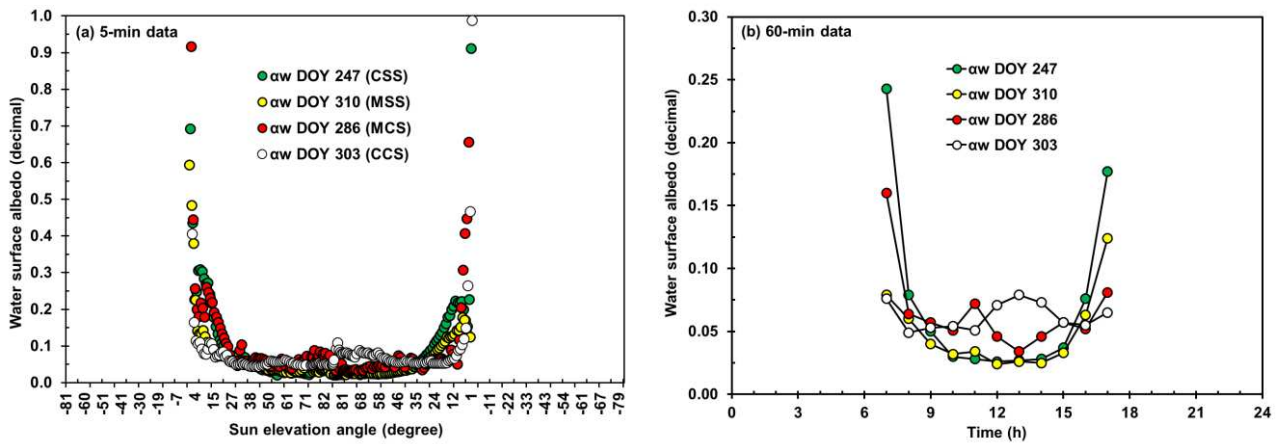


**Fig. 6 a, b** Daily course of the low-turbidity water albedo  $\alpha_w$  for the four selected days with contrasting cloud cover. DOY 247/2015 (CSS,  $\tau_{\text{atm}} = 0.72$ ), DOY 310/2016 (MSS,  $\tau_{\text{atm}} = 0.55$ ), DOY 286/2016 (MCS,  $\tau_{\text{atm}} = 0.36$ ), and DOY 303/2015 (CCS,  $\tau_{\text{atm}} = 0.18$ ). CSS = completely sunny (clear) sky, MSS = mostly sunny sky, MCS = mostly cloudy sky, and CCS = completely cloudy (overcast) sky

471

472 Figure 6b illustrates how cloud cover affected the daily course of  $\alpha_w$ . U-shape curves are seen on clear and near clear  
 473 days (DOY 247 and 310), with maximums occurring early in the morning and late afternoon when sun angles were low,  
 474 and minimums occurring around noon when sun angles were highest. Under high atmospheric transmissivity, a well-  
 475 defined relationship between water albedo and time was observed (Nunez et al. 1972; Henderson-Sellers 1986; Liu et al.  
 476 2015). On the other hand, Fig. 6b shows that as the degree of cloudiness increased, the U-shape pattern changed so that the  
 477 timing of maximum and minimum  $\alpha_w$  values became more difficult to predict and  $\alpha_w$  amplitude decreased. For the four  
 478 cloud cover conditions, the mean daily albedo computed using the daily values of  $S_g$  and  $S_r$  from Table 3 were 0.045 (DOY  
 479 247), 0.038 (DOY 310), 0.054 (DOY 286), and 0.061 (DOY 303), with an overall average of 0.049. The days in Fig. 6  
 480 comprise a representative range of conditions for the mean daytime atmospheric transmissivity (0.18-0.72), so it is expected  
 481 that the average  $\alpha_w$  for these days is similar to that calculated from all data for both 2015 and 2016 seasons (see comments  
 482 related to Fig. 3b).

483 Because albedo varies over the course of a day, Table 5 shows adjustments of a power-law model from which  $\alpha_w$  is  
 484 estimated from  $\theta$  and from incoming SW radiation, which by itself is also a function of  $\theta$ . 5-min average data were used to  
 485 calibrate the model. Generally, the coefficient of determination ( $r^2$ ) decreased as cloud cover increased. Considering the  
 486 all-cloud cover condition case in Table 5, the model predicts  $\alpha_w$  varying from 0.25 to 0.03 in the  $\theta$  interval from  $5^\circ$  to  $90^\circ$ .  
 487 These estimated values are within the range of measured albedo over the low-turbidity water during both the 2015 and  
 488 2016 seasons.

489

490

491

492

493 **Table 5** Coefficients for the power-law fitting relationship for estimating the low-turbidity water surface albedo ( $\alpha_w$ ) in a  
 494 tropical climate from incident SW radiation flux ( $S_g$ ) in  $W\ m^{-2}$  and sun elevation angle ( $\theta$ ) in degree

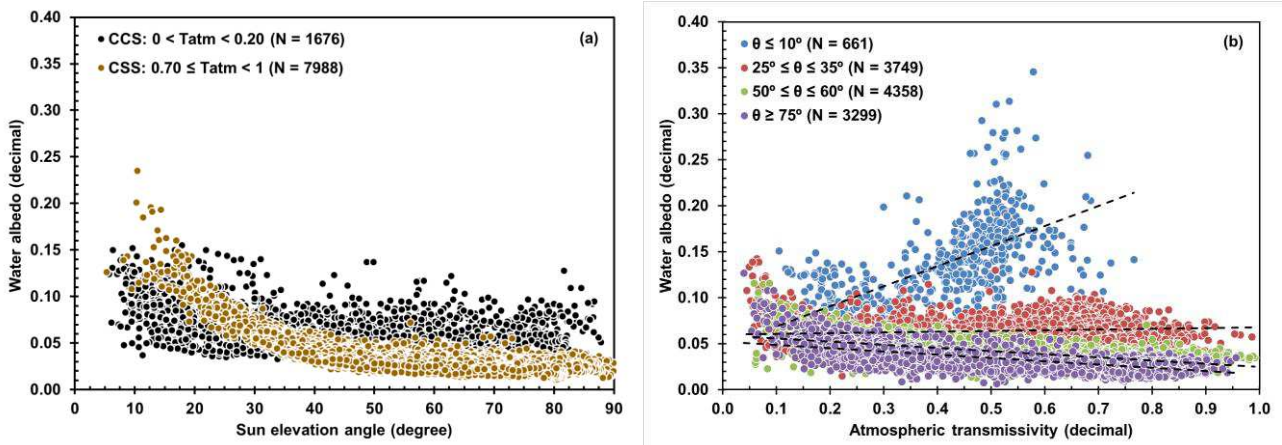
Cloud cover conditions	$\alpha_w = A \cdot (\theta)^B$			$\alpha_w = C \cdot (S_g)^D$		
	A	B	$r^2$	C	D	$r^2$
All	0.8563	-0.771	0.70	1.1324	-0.521	0.53
CSS	1.3842	-0.931	0.68	75.552	-1.147	0.67
MSS	1.5587	-0.921	0.86	28.594	-1.019	0.83
MCS	0.2938	-0.469	0.56	0.6849	-0.461	0.48
CCS	0.1524	-0.239	0.20	0.3104	-0.335	0.36

495 CSS = completely sunny (clear) sky, MSS = mostly sunny sky, MCS = mostly cloudy sky, and CCS = completely cloudy (overcast) sky  
 496

497 Figure 7a illustrates, for the two extremes cases of cloud cover (CCS vs. CSS), the variation of  $\alpha_w$  with  $\theta$  based on the  
 498 5-min data sets from both years as found in the datalogger table. Before processing the raw data, filters were applied as  
 499 follows: (i) all data were deleted from the series when the calculated  $\tau_{atm}$  was not a value,  $\tau_{atm} \leq 0$  or  $\tau_{atm} \geq 1$ ; (ii) all data  
 500 were deleted when calculated  $\theta$  was not a value or  $\theta \leq 0$ ; (iii) all data were deleted when  $\alpha_w$  was not a value or when  $\alpha_w \leq$   
 501 0, and  $\alpha_w > 1$ ; and (iv) all data were deleted when  $R_n < 0$ . Fig. 7a shows the values for valid points after applying this  
 502 quality control.

503 As previously discussed in Fig. 6 and according to Katsaros et al. (1985) and Jin et al. (2004), Fig. 7a illustrates that  
 504 under high sun elevation above the horizon and with flat water surface, the albedo for water tends to be higher in the  
 505 presence of clouds (overcast and near overcast skies), as the diffuse, multi-direction SW radiation in the atmosphere  
 506 increases the mean angle of incidence of radiation from the vertical and the effect of solar elevation is considerably  
 507 dampened (Oke, 1995). In the absence of clouds (clear sky and near clear sky) the incidence angle is small and the albedo  
 508 is lowest. The opposite occurs when the sun is low above the horizon ( $\theta < 30^\circ$ ). In this condition, the albedo tends to be  
 509 larger in the absence of clouds at low sun angle and increases sharply with sun angle, as the angle of incidence of the  
 510 radiation beam from vertical becomes greater.

511



512 **Fig. 7 a, b** Plot of low-turbidity water albedo against sun elevation angle for the two extreme conditions of cloud cover  
 and against atmospheric transmissivity for SW radiation for four intervals of sun elevation angle

513

514 Figure 7a also shows that, for a given sun elevation angle, the variability in  $\alpha_w$  under dense cloud cover was  
 515 substantially higher. This higher variability can be a combined effect of the state of the surface (lack of flatness due to  
 516 wind blowing) and diffuse radiation reaching the surface in larger proportions compared to the direct beam. For the CCS  
 517 condition in Fig. 7a, 5-min albedo calculated from values of incoming SW radiation ( $S_g$ ) ranged from  $21.0\ W\ m^{-2}$  to  $270.3$   
 $W\ m^{-2}$  and reflected SW radiation ( $S_r$ ) varied from  $2.1\ W\ m^{-2}$  to  $19.9\ W\ m^{-2}$ . The highest values for albedo ( $> 0.10$ )

518 corresponded to 8.5% of the total points, with  $S_g$  and  $S_r$  lying within the intervals from  $21.0 \text{ W m}^{-2}$  to  $131.2 \text{ W m}^{-2}$  and  $2.9$   
 519  $\text{W m}^{-2}$  to  $14.1 \text{ W m}^{-2}$ .

520 It is interesting to observe in Fig. 7a that from around  $25^\circ$  to  $35^\circ$  of sun elevation, the two extreme cloud cover data  
 521 sets tended to intersect and the relationship between  $\alpha_w$  and  $\theta$  seems to have been less dependent on the degree of cloudiness.  
 522 A second plot (Fig. 7b) was developed to explore how water albedo relates to the full range of atmospheric transmissivity  
 523 ( $\tau_{\text{atm}}$ ) for a set of arbitrarily chosen  $\theta$  intervals. In Fig. 7b, the albedo of the low turbidity water was very sensitive to changes  
 524 in  $\tau_{\text{atm}}$  under low sun elevation angle ( $\theta \leq 10^\circ$ ). In this range,  $\alpha_w$  increased rapidly as  $\tau_{\text{atm}}$  increased, most likely due to larger  
 525 sunglint from the greater amount of direct sun beam at higher  $\tau_{\text{atm}}$ . In the  $25^\circ$  to  $30^\circ$  range,  $\alpha_w$  was essentially constant  
 526 across the  $\tau_{\text{atm}}$  values. At higher  $\theta$  values ( $> 50^\circ$ ), the water albedo shows a slightly decreasing pattern with atmospheric  
 527 transmissivity with lowest values of  $\alpha_w$  toward clear sky in accordance with Fig. 7a.

528

### 529 3.5 Models for estimating net radiation fluxes

530

531 Modelling net radiation fluxes from commonly measured weather data makes the determination of radiation balance over  
 532 surfaces more viable and independent of high-cost and delicate instrumentation. It also increases the ability to apply the  
 533 methodology using historical data sets. The proposed approach to predict net SW radiation for the low-turbidity water (Eq.  
 534 (5)) is simplified and made more general by requiring only a knowledge of  $\alpha_{\text{wc}}$ , as a constant value for water albedo as  
 535 previously defined. On a daily basis, the  $\alpha_{\text{wc}}$  adopted here is 0.05, which is about the average water surface albedo calculated  
 536 for both 2015 and 2016 from 24-hr  $S_g$  and  $S_r$  fluxes (see section 3.3 *Seasonal analysis of radiation balance components*).  
 537 This value was also obtained from measured  $S_{\text{net}}$  data (totaling 189 points of daily data from both years). Data were plotted  
 538 against  $S_{\text{net}(e)}$  and the albedo was varied until the best fitting ( $Y = 1.0007 \cdot X$ ,  $r^2 = 0.99996$ , and  $\text{SEE} = 1.53 \text{ W m}^{-2}$ ) was  
 539 obtained, which occurred when  $\alpha_{\text{wc}}$  was set equal to 0.047 or about 0.05. Following the determination of an appropriate  
 540 constant value for albedo, the net SW radiation flux was then modelled from  $S_g$  measured at the weather station as  $S_{\text{net}(e)} =$   
 541  $0.95 \cdot S_g$ , which means that on average, 95% of the daily SW radiation incident over the water surface in the clear irrigation  
 542 reservoirs was absorbed. Therefore, compared to other natural surfaces, liquid water is on average one of the most effective  
 543 absorbing mediums of SW solar radiation (Oke, 1995; Katsaros et al. 1985; Jensen and Allen 2016).

544 As shown previously, two approaches were applied to model net LW radiation, the FAO56 equation (Eq. (6)) and a  
 545 multiple linear regression model (Eq. (7)) using atmospheric variables commonly collected at a standard automatic weather  
 546 station. The inputs to the FAO56  $L_{\text{net}}$  model (Allen et al. 1998) are  $T_x$  (maximum air temperature, K),  $T_n$  (minimum air  
 547 temperature, K),  $e_a$  (actual vapor pressure, kPa), and the  $S_g/S_{\text{go}}$  ratio (relative cloudiness index, dimensionless). Based on  
 548 daily data from 2015 (totaling 134 data points), it was found that  $L_{\text{net}(56)}$  underestimated measured values for water by about  
 549 30%, with a mean ratio between estimated and measured  $L_{\text{net}}$  equal to 0.70 (max = 1.32, min = 0.18, standard deviation, sd  
 550 = 0.18). Measured  $L_{\text{net}(56)}$  was plotted against calculated values resulting in a linear regression fitting ( $Y = A + B \cdot X$ ) with  
 551 the following parameters:  $A = 24.91 \text{ W m}^{-2}$ ,  $B = 0.7734$ ,  $r^2 = 0.608$ , and  $\text{SEE} = 7.99 \text{ W m}^{-2}$ . One data point (30<sup>th</sup> October)  
 552 was excluded from this analysis because the condition of  $S_g/S_{\text{go}} > 0.25$  was violated.

553 The same 2015 set of daily data ( $N = 135$ ) was used to derive the coefficients for the multiple linear regression (MLR)  
 554 model. Several weather variables commonly associated to the exchange of LW radiation between surface and atmosphere  
 555 were considered, such as  $T_x$  ( $^\circ\text{C}$ ),  $T_n$  ( $^\circ\text{C}$ ),  $e_a$  (kPa),  $S_g/S_{\text{go}}$  (dimensionless), mean air temperature ( $T_m$ ,  $^\circ\text{C}$ ) given as  $(T_x +$   
 556  $T_n)/2$ , maximum relative humidity ( $\text{RH}_x$ , %), minimum relative humidity ( $\text{RH}_n$ ), air temperature amplitude ( $\Delta T$ ,  $^\circ\text{C}$ ), and  
 557 vapor pressure deficit (VPD, kPa). Fourth-degree powers of  $T_x$  and  $T_n$  were also considered, as in the FAO56 model

558 following the Stefan-Boltzmann law. These variables were tested as a single input and in pairs in the form of products.  
 559 After many runs, the best fitting relationship ( $r^2 = 0.721$ ,  $SEE = 6.87 \text{ W m}^{-2}$ ) was obtained when measured daily  $L_{net}$  was  
 560 expressed as a function of  $T_x$  ( $^{\circ}\text{C}$ ),  $T_n$  ( $^{\circ}\text{C}$ ),  $RH_x$  (%),  $RH_n$  (%), and  $S_g/S_{go}$  according to Eq. (11), limited to  $6 \text{ W m}^{-2} \leq L_{net(56)}$   
 561  $\leq 60 \text{ W m}^{-2}$ ;

562

$$L_{net(MLR)} = 8.661 + 1.077(T_x) - 3.334(T_n) + 0.947(RH_x) - 0.480(RH_n) + 26.869 \left( \frac{S_g}{S_{go}} \right) \quad (11)$$

563

564 Different from the FAO56 model, in Eq. (11) the  $S_g/S_{go}$  ratio is allowed to be lower than or equal to 0.30 since values  
 565 in this range were used for derivation. Validation of  $L_{net(MLR)}$  against daily data obtained in 2016 ( $N = 54$  for independent  
 566 data points) showed a linear regression fitting through the origin ( $Y = B \cdot X$ ) with a high coefficient of determination ( $r^2 =$   
 567  $0.986$ ), slope near 1 ( $B = 0.981$ ), and a small standard error of estimate ( $SEE = 6.76 \text{ W m}^{-2}$ ).

568 Figure 8 depicts the course of measured and estimated net LW radiation for year 2016 by both methods. This plot is a  
 569 form of validation for the FAO56 approach that could not be done in the same way that was done for the multiple linear  
 570 regression. It is interesting to observe that both sets of estimated data not only agree with each other, but also agree with  
 571 the measured values for  $L_{net}$ . Basically, both FAO56 and MLR approaches concomitantly produced an overestimation or  
 572 underestimation for measured  $L_{net}$ , with the MLR curve closer to measured  $L_{net}$  most of the time, for example, from DOY  
 573 172 to DOY 175. The ratio between estimated and measured  $L_{net}$  in 2016 was on average 0.63 (max = 0.91, min = 0.11, sd  
 574 = 0.16) for the FAO56 model and 1.04 (max = 1.79, min = 0.80, sd = 0.16) for the MLR model. Therefore, the use of Eq.  
 575 (11) to estimate the net outgoing LW radiation over the low turbidity water seems to be a better option as compared to the  
 576 FAO 56 model, since the regression is tailored to the experimental data.

577

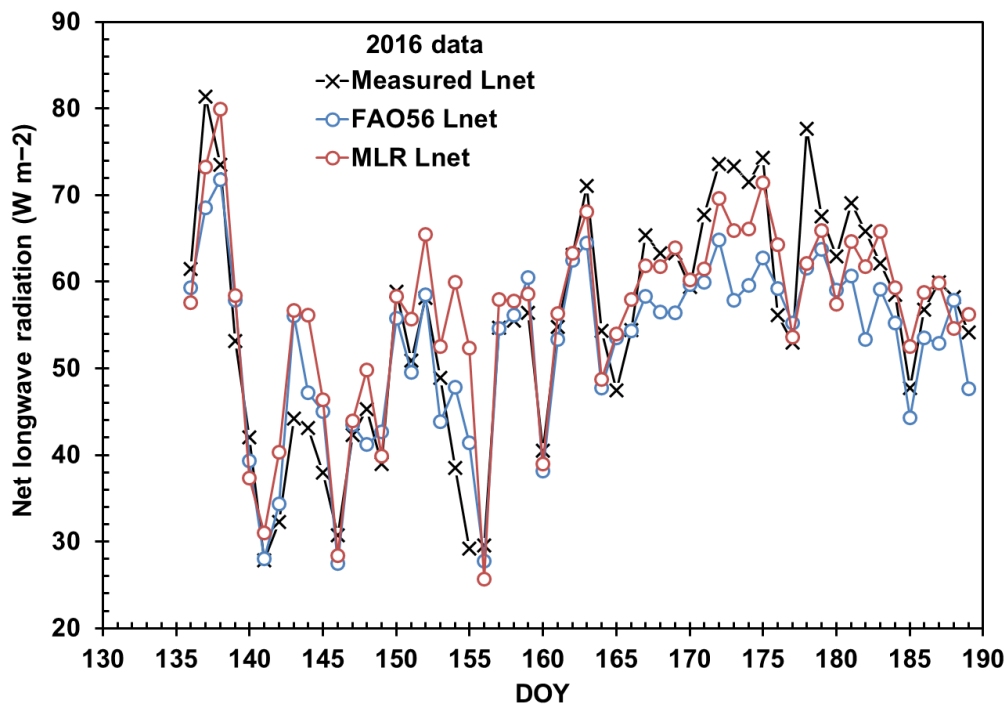


**Fig. 8** Course of measured and estimated daily net longwave radiation over the low-turbidity water surface in 2016 from DOY 136 to DOY 189 (54-day interval).

578

579 The FAO56 equation (Eq. (6)) for estimating  $L_{net}$  was developed for vegetated surfaces in the context of crop water  
 580 requirement studies (Wright, 1982; Burman and Pochop 1994; Allen et al. 1998). That equation assumes an emissivity of  
 581 0.98 for the soil-vegetation mixture and the calculation of net emissivity with the Brunt (1932) model, which is a value  
 582 similar to that recommended for water surfaces ( $\epsilon_w = 0.97$ ) (Davies et al. 1971; Konda et al. 1994; Jensen and Allen 2016).  
 583 On the other hand, the FAO56 equation uses air temperature at screen height to estimate both incoming and outgoing LW  
 584 radiation and the equation is applied to hourly and daily calculations of reference evapotranspiration (Jensen et al., 1990;  
 585 Jensen and Allen 2016). Figure 5 shows that, under the same environmental conditions, differences between  $T_w$  and  $T_a$  can  
 586 be significant. Such differences might explain the inability of the FAO56 equation to predict  $L_{net}$  over the low turbidity  
 587 water surface in the experimental area of this study. In order to improve the FAO56  $L_{net}$  model, one option would be to  
 588 adjust the coefficients for net emissivity and the cloud cover factor to account for local conditions (Kjaersgaard et al. 2007;  
 589 Kofronova et al. 2019), which is desirable since this formulation of  $L_{net}$  based on the Stefan-Boltzmann law and the concept  
 590 of a net emissivity with the Brunt equation has been successfully applied over a large range of cropped and surfaces. Such  
 591 adjustment was not attempted in this study, since the objective was to test the FAO model as is.

592 Net all-wave radiation ( $R_n$ ) was modelled following three approaches (Eq. (8) – Eq. (10)). In the first approach,  $S_{net(e)}$   
 593  $= 0.95 \cdot S_g$  was taken as the predictor variable and Eq. (12) is the result of the linear regression analysis that produced a  
 594 model with a high correlation ( $r^2 = 0.951$  and  $SEE = 9.66 \text{ W m}^{-2}$ ), since net radiation is closely correlated with net SW  
 595 radiation, which in turn is closely correlated with incoming SW radiation (Fig. 3 and Fig. 4). Derivation of Eq. (12) used  
 596 data from 2015 ( $N = 135$ ) and was restricted to  $S_{net(e)}$  values from about  $79 \text{ W m}^{-2}$  to  $306 \text{ W m}^{-2}$ . Validation with the 2016  
 597 data set ( $N = 54$ ) showed a linear model passing through the origin ( $Y = B \cdot X$ ) with  $B = 1.034$ ,  $r^2 = 0.998$ , and  $SEE = 7.56$   
 598  $\text{W m}^{-2}$ .

599

$$R_{n(1)} = -21.357 + 0.832 \cdot S_{net(e)} \quad (12)$$

600

601 Figure 9 compares measured daily  $R_n$  with calculated values obtained with approach  $R_{n(2)}$  (Eq. (9)) where the net LW  
 602 radiation flux was estimated using  $L_{net(56)}$  and with approach  $R_{n(3)}$  (Eq. (10)) where the net LW radiation flux was given by  
 603  $L_{net(MLR)}$ . A better agreement between measured and estimated  $R_n$  was obtained with  $R_{n(3)}$  where the y-intercept is closer to  
 604 0 and the slope is closer to 1 and with  $SEE$  equal to  $7.37 \text{ W m}^{-2}$ , which is 33% lower than the  $SEE$  in Fig. 9a. Therefore, it  
 605 is recommended that net all-wave radiation flux be estimated with approach  $R_{n(3)}$  for the clear type of water stored in the  
 606 irrigation storage tanks of the tobacco farm. The ratio of  $R_{n(2)}$  to  $R_n$  averaged 1.13 and 1.01 for the  $R_{n(3)}$  to  $R_n$  ratio.

607

608

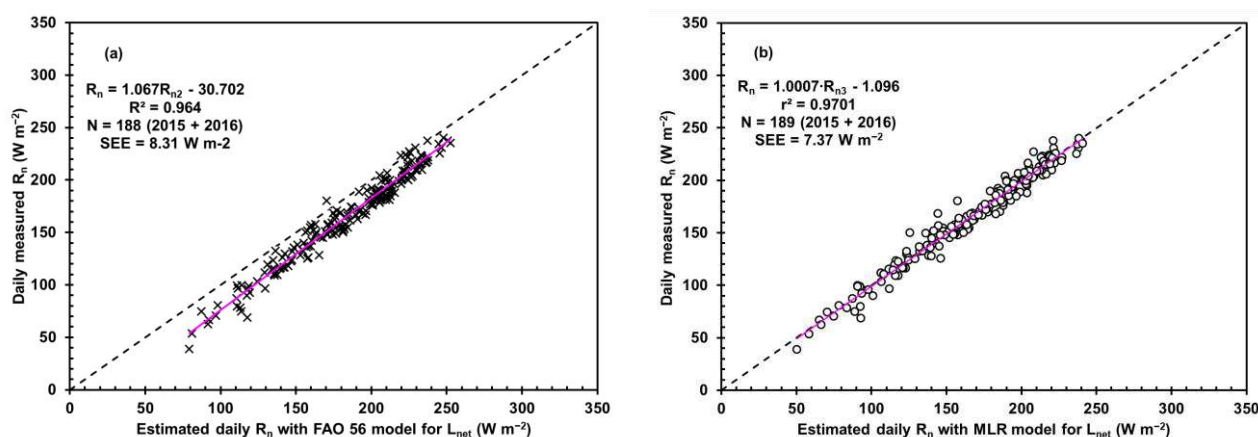


**Fig. 9 a, b** Measured all-wave net radiation against calculated net-all wave radiation with  $L_{net(56)}$  (a) and as  $L_{net(MLR)}$ , where 56 stands for FAO 56 Penman-Monteith equation and MLR stands for multiple linear regression model

609

610

611 The use of a well-fitted simple linear regression to estimate  $R_n$  over water surface in terms of incoming SW radiation  
 612 or net SW radiation is a valid option where data on solar radiation are available and the water quality remains fairly constant  
 613 over time, which is the case of the experimental area of this study. In the tobacco farm, every year from April to August,  
 614 the tanks are refilled with clean water coming from the filtration system to supply crop demand during the next irrigation  
 615 season. If a local or regional automatic weather station provides data on other parameters such as air temperature (maximum  
 616 and minimum) and relative humidity (maximum and minimum) that can be provided to a MLR model for  $L_{net}$  then the  $R_{n(3)}$   
 617 approach becomes another option for calculation of net radiation over the water surfaces in the farm.

618

## 619 4 Conclusions

620

621 In this study, data on turbidity, radiation balance, and skin temperature were analyzed from measurements made in the  
 622 center of a farm pond that stored low-turbidity water for irrigation of a special variety of tobacco in eastern Bahia, Brazil.  
 623 A standard automatic weather station was deployed in the experimental area to provide auxiliary data. A turbidimeter, a  
 624 four-component net radiometer, and an infrared thermometer were installed during the irrigation seasons of 2015 and 2016  
 625 on board a handmade floating platform (raft) in which sensors, datalogger, and power supply equipment were deployed.  
 626 Valid water turbidity readings were obtained only during the 2016 season, and remained at very low (2.6 NTU on average).

627 The shortwave (SW) components for the radiation balance were strongly affected by daytime cloudiness evaluated  
 628 using the atmospheric transmissivity ( $0 < \tau_{atm} < 1$ ) calculated as the ratio of incoming shortwave (SW) at the surface ( $S_g$ )  
 629 to that at the top of the atmosphere ( $S_o$ ). The absorption of SW radiation by water was high and corresponded to about 96%  
 630 of  $S_g$  (2015 + 2016). During both seasons, daily longwave (LW) emission upward from the water surface ( $L_e$ ) remained  
 631 higher than that for downward radiation from the atmosphere ( $L_{atm}$ ), making the net LW radiation ( $L_{net}$ ) consistently  
 632 negative ( $-55.1 \text{ W m}^{-2}$  on average). The net all-wave radiation ( $R_n$ ) corresponded to 77% of net SW radiation ( $S_{net}$ ),  
 633 evidencing a smaller contribution from  $L_{net}$  to  $R_n$ . Seasonal water surface albedo ( $\alpha_w$ ) averaged about 0.05 on a daily basis,  
 634 as calculated from 24 h mean values of reflected SW radiation ( $S_r$ ) and  $S_g$ .

635 Analysis on four selected days of contrasting  $\tau_{atm}$  (0.72 – clear sky, 0.55, 0.36, and 0.18 – overcast sky) showed that  
 636 the degree of cloudiness decreased  $S_g$  by 70% while the effect on  $L_{atm}$  was the opposite, increasing by 14%. The  $S_{net}$  and  
 637  $S_r$  components in the radiation balance decreased with cloud cover, following the same trend in  $S_g$ , resulting in 70.5% and

638 59% reductions, respectively. Longwave radiation reflected by water ( $L_r$ ) followed the same trend for  $L_{atm}$  across the four  
 639 days since a constant emissivity of 0.03 was utilized. The  $L_e$  component showed no trends with cloud cover and differences  
 640 among the four days and were small ( $11 \text{ W m}^{-2}$  range) due to the relatively constant water surface temperature over the 24  
 641 periods. The behavior of outgoing LW radiation ( $L_r + L_e$ ) showed no trends with cloud cover relative to the behavior of  
 642  $L_{atm}$  with  $L_{net}$  also decreasing with the degree of cloudiness, with a reduction of about 54%.  $R_n$  followed  $S_g$  very closely  
 643 regardless the degree of cloud cover with  $R_n$  experiencing a reduction of about 78% from the clear to the overcast sky.  
 644 Within the course of a day, the  $L_e$  and  $L_{atm}$  components experienced slight variation over 24 h, but, in general, for all four  
 645 days, both atmospheric and water LW emission varied little as cloud cover increased.

646 The measurement of air and water surface temperature ( $T_a$  and  $T_w$ , respectively) in 2015 (having a longer measurement  
 647 season with 135 days) revealed that  $T_a$  was consistently below  $T_w$  except during afternoon when  $T_a$  peaked above  $T_w$   
 648 for most of the days of the period. In all days, the daily amplitude in  $T_a$  was higher than that for  $T_w$ . During the 2015 season,  
 649 daily mean  $T_w$  was  $26.1 \text{ }^\circ\text{C}$  (max =  $29.0 \text{ }^\circ\text{C}$ , min =  $23.3 \text{ }^\circ\text{C}$ ) and daily mean  $T_a$  on the order of  $21.8 \text{ }^\circ\text{C}$  (max =  $26.3 \text{ }^\circ\text{C}$ , min  
 650 =  $18.7 \text{ }^\circ\text{C}$ ). The resistance of water to changing temperature is due to its higher heat capacity ( $4180 \text{ kJ m}^{-3} \text{ K}^{-1}$ ), coupled  
 651 with water depth, as compared to air ( $1.2 \text{ kJ m}^{-3} \text{ K}^{-1}$  at  $25 \text{ }^\circ\text{C}$ ). The impact of cloud cover on daily variation in  $T_a$  and  $T_w$   
 652 for the four selected days of contrasting  $\tau_{atm}$  revealed that the two temperatures did not follow any particular trend with  
 653 cloud cover, which suggests that average temperature near or at the water surface cannot be solely explained based on  
 654 degree of cloudiness. However, this was not the case for the temperature amplitude ( $\Delta T$ ), because for both water and air,  
 655  $\Delta T$  decreased as cloud cover increased. Regardless of cloud cover, the overall average for  $T_w$  ( $26.8 \text{ }^\circ\text{C}$ ) was higher than  
 656 for  $T_a$  ( $23.2 \text{ }^\circ\text{C}$ ). In general, not only did the air show higher temperature variation over 24 h as compared to the low-  
 657 turbidity water, but  $T_w$  was higher than  $T_a$  most of the time, especially at nighttime.

658 For any condition of atmospheric transmissivity (0.72 – clear sky, 0.55, 0.36, and 0.18 – overcast sky) the water surface  
 659 albedo ( $\alpha_w$ ) tended to decrease as sun elevation angle  $\theta$  increased in the  $0$  to  $90^\circ$  range. Under clear sky there was a well-  
 660 defined U-shape pattern for  $\alpha_w$  from sunrise to sunset, with a maximum  $\alpha_w$  occurring at low  $\theta$  and a minimum at high sun  
 661 elevation. This pattern was not observed under near overcast or overcast skies, where, as cloud cover increased, both the  
 662 timing of the maximum and minimum  $\alpha_w$  values became more difficult to predict, and the amplitude of albedo decreased.  
 663 A power law model was fitted to 5-min data to express  $\alpha_w$  as a function of  $\theta$  and in terms of  $S_g$  as well. The model for all  
 664 cloud cover conditions with  $r^2$  around 0.70 predicted  $\alpha_w$  varying from 0.25 to 0.03 over the  $5^\circ$  to  $90^\circ$  interval for  $\theta$ . These  
 665 values are within the range of measured albedo over both seasons. Filtered 5-min raw data of  $\alpha_w$  plotted against atmospheric  
 666 transmissivity ( $\tau_{atm}$ ) for four arbitrarily chosen  $\theta$  intervals showed that for  $\theta$  ranging from  $25^\circ$  to  $35^\circ$ , the water surface  
 667 albedo showed a constant trend over the full range of  $\tau_{atm}$  (0 to 1). For a lower  $\theta$  interval ( $\leq 10^\circ$ ),  $\alpha_w$  increased rapidly with  
 668 increasing  $\tau_{atm}$ . For two higher  $\theta$  intervals ( $50 \leq \theta \leq 60$  and  $\theta \geq 75^\circ$ ),  $\alpha_w$  decreased slowly with increasing  $\tau_{atm}$  with the  
 669 lowest values of  $\alpha_w$  toward clear sky conditions.

670 Modelling the net radiation fluxes over the low-turbidity water surface showed that  $S_{net}$  can be modelled from daily  $S_g$   
 671 measured at a nearby weather station as  $0.95 \cdot S_g$ , which means that a constant water albedo of 0.05 can be recommended  
 672 for the very clear water conditions of this study.  $L_{net}$  can be estimated with good accuracy ( $r^2 = 0.72$ ,  $SEE = 6.87 \text{ W m}^{-2}$ )  
 673 from a multiple linear regression model (MLR) fitted with the 2015 data having five inputs typically related to the LW  
 674 exchange between the atmosphere and the surface, i.e., maximum and minimum air temperature ( $T_x$ ,  $T_n$ ,  $^\circ\text{C}$ ), maximum  
 675 and minimum air relative humidity ( $RH_x$ ,  $RH_n$ , %), and the relative daytime cloudiness ( $S_g/S_{go}$ , dimensionless). Validation  
 676 of  $L_{net(MLR)}$  against 2016 daily data showed a linear regression fitting through the origin ( $Y = B \cdot X$ ) characterized by  $r^2 =$   
 677  $0.986$ ,  $B = 0.981$ , and  $SEE = 6.76 \text{ W m}^{-2}$ . The FAO56 net LW radiation approach was also tested with the 2015 data and

678 revealed an underestimation of daily  $L_{\text{net}}$  with a mean ratio between estimated and measured values equal to 0.70 (max =  
 679 1.32, min = 0.18). When measured  $L_{\text{net}}$  was plotted against  $L_{\text{net}(56)}$  the result was a linear regression fitting ( $Y = A + B \cdot X$ )  
 680 with the following parameters:  $A = 24.91 \text{ W m}^{-2}$ ,  $B = 0.7734$ ,  $r^2 = 0.61$ , and  $\text{SEE} = 7.99 \text{ W m}^{-2}$ . Differences between  
 681 measured  $L_{\text{net}}$  and  $L_{\text{net}(56)}$  can be explained by the assumptions behind the FAO56 approach, mainly in the fact that a single  
 682 temperature at screen height is assumed for both air and surface temperature. Improvements in the FAO56 approach can  
 683 be obtained by adjusting coefficients to local conditions the coefficients of the cloud cover factor, which is desirable since  
 684 this approach has been successfully applied over a large range of natural surfaces mainly soil-vegetation mixtures. Two  
 685 options resulted for estimating daily net all-wave radiation  $R_n$  over the low turbidity water in the tobacco farm: (a)  $R_n = -$   
 686  $27.357 + 0.832 \cdot S_{\text{net}(e)}$  ( $r^2 = 0.998$  and  $\text{SEE} = 9.66 \text{ W m}^{-2}$ ) where  $S_{\text{net}(e)} = 0.95 \cdot S_g$  and (b)  $R_n = S_{\text{net}(e)} - L_{\text{net(MLR)}}$ . Both options  
 687 use data readily collected at standard automatic weather stations.

688

689 **Conflict of interest** The authors declare that they have no conflict of interest.

690 **Funding statement** The authors manifest their appreciation to the *Fundação de Amparo à Pesquisa*  
 691 *do Estado da Bahia / State of Bahia Foundation for Scientific Research* (FAPESB) for the financial  
 692 support through a research grant (TO APP0075/2011) and doctorate scholarship (TO BOL0545/2013)  
 693 to the first author without which this research would not have been possible. Support from the Idaho  
 694 Agricultural Experiment Station (IDA01620) and Nebraska Agricultural Experiment Station is  
 695 acknowledged.

696 **Author's contribution:** Conceptualization, Methodology, and Formal analysis and investigation  
 697 (Aureo Silva de Oliveira, Tatyana Keyty de Souza Borges, Richard G. Allen), Writing – original  
 698 draft preparation (Tatyana Keyty de Souza Borges, Aureo Silva de Oliveira), Writing – review and  
 699 editing (Aureo Silva de Oliveira, Richard G. Allen, Ayse Kilic), Funding acquisition (Aureo Silva de  
 700 Oliveira, Richard G. Allen), Resources (Aureo Silva de Oliveira, Tatyana Keyty de Souza Borges,  
 701 Carlos Eduardo Santana, João Paulo Chaves Couto); Data collection (Tatyana Keyty de Souza  
 702 Borges, Aureo Silva de Oliveira, João Paulo Chaves Couto)

703 **Availability of data and material:** not apply

704 **Code availability:** not apply

705 **Ethics approval:** not apply

706 **Consent to participate:** All authors participated in the work of their own free will.

707 **Consent for publication:** All authors read and approved the final manuscript for publication,  
 708 including the names and order of authors.

709

## 710 **References**

- 711 Ai Z, Yang Y, Wang Q, Han S, Yang Y, Wang Q, Qiu G (2018) Changes of surface energy partitioning caused by plastic  
 712 mulch in a cotton field. *Int Agrophys* 32(3):349–356
- 713 Akritas, M (2016) *Probability and statistics with R for engineers and scientists*. New York, Pearson

- 714 Alados I, Foyo-Moreno I, Olmo FJ, Alados-Arboledas L (2003) Relationship between net radiation and solar radiation for  
715 semi-arid shrub-land. *Agric For Meteorol* 116(3):221–227
- 716 Allen RG (1996) Assessing integrity of weather data for reference evapotranspiration estimation. *J Irrig Drain Eng*  
717 122(2):97–106
- 718 Allen RG, Pereira LS, Raes D, Smith M (1998) Crop evapotranspiration: guidelines for computing crop water requirements.  
719 United Nations FAO, Irrigation and Drainage Paper 56
- 720 Alvares CA, Stape JL, Sentelhas PC, Gonçalves JL de M, Sparovek G (2013) Koppen’s climate classification map for  
721 Brazil. *Meteorol Zeitschrift* 22(00):711–728
- 722 Aydin H, Karakus H (2016) Estimation of evaporation for Lake Van. *Environ Earth Sci* 75(18):1275
- 723 ASCE (2005) The ASCE standardized reference evapotranspiration equation. ASCE, Reston
- 724 Bilbao J, De Miguel AH (2007) Estimation of daylight downward longwave atmospheric irradiance under clear-sky and  
725 all-sky conditions. *J Appl Meteorol Climatol* 46:879-889
- 726 Blonquist Jr JM, Tanner BD, Bugbee BD (2009) Evaluation of measurement accuracy and comparison of two new and  
727 three traditional net radiometers. *Agric For Meteorol* 149(10):1709-1721
- 728 Borges TKS (2017) Evaporação em superfície de água livre com baixa turbidez. Universidade Federal do Recôncavo da  
729 Bahia, Brazil. PhD Dissertation (in Portuguese)
- 730 Borges TKS, Oliveira AS de, Silva ND da, Santana CE (2016) Plataforma flutuante de baixo custo para pesquisas em  
731 micrometeorologia e qualidade da água em reservatórios. *Revista Geama* 4(1):38-45 (in Portuguese)
- 732 Burman R, Pochop LO (1994) Evaporation, evapotranspiration, and climatic data. Amsterdam, Elsevier (Developments in  
733 Atmospheric Science, 22)
- 734 Brunt D (1932) Notes on radiation in the atmosphere. *Quart J Roy Meteorol Soc* 58:389-418
- 735 Campbell Scientific (2014) CNR4 net radiometer instruction manual. <https://s.campbellsci.com>. Accessed 23 October 2015
- 736 Campbell GS and Norman JM (1998) An introduction to environmental biophysics. 2<sup>nd</sup> ed. Springer, New York
- 737 Carmona F, Rivas R, Caselles V (2014) Estimation of daytime downward longwave radiation under clear and cloudy skies  
738 conditions over a sub-humid region. *Theor Appl Climatol* 115(1-2):281-295
- 739 Cogley, JG (1979) The albedo of water as a function of latitude. *Mon Weather Rev* 107(6):775-781
- 740 Davies JA, Robison PJ, Nunez M (1971) Field determinations of surface emissivity and temperature for Lake Ontario. *J*  
741 *Appl Meteorol* 10(4):811-819
- 742 Davies-Colley RJ, Smith DG (2001) Turbidity, suspended sediment, and water clarity: A review. *J Am Water Resour As*  
743 37(5):1085-1101
- 744 Downing JA, Prairie YT, Cole JJ, Duarte CM, Tranvik LJ, Striegl RG, McDowell WH, Kortelainen P, Caraco NF, Melack  
745 JM, Middleburg JJ (2006) The global abundance and size distribution of lakes, ponds, and impoundments. *Limnol*  
746 *Oceanogr* 51(5):2388-2397
- 747 El Bakry MM (1994) Net radiation over the Aswan High Dam Lake. *Theor Appl Climatol* 49(3):129-133
- 748 Feng Y, Liu Q, Qu Y, Liang S (2016) Estimation of the ocean water albedo from remote sensing and meteorological  
749 reanalysis data. *IEEE Trans Geosci Remote Sens* 54(2):850-868.
- 750 Field RT, Fritschen LJ, Kanemasu ET, Smith EA, Stewart JB, Verma SB, Kustas WP (1992) Calibration, comparison, and  
751 correction of net radiation instruments used during FIFE. *Journal of Geophysical Research* 97(D17):18,681-18,695
- 752 Finch JW, Hall RL (2005) Evaporation from lakes. In: Anderson MG, McDonnell JJ (ed) *Encyclopedia of hydrological*  
753 *sciences*. Wiley, Chichester, pp. 635-646

- 754 Gallego-Elvira B, Baille A, Martín-Górriz B, Martínez-Álvarez V (2010) Energy balance and evaporation loss of an  
755 agricultural reservoir in a semi-arid climate (south-eastern Spain). *Hydrol Process* 24(00):758-766
- 756 Gianniou SK, Antonopoulos VZ (2007) Evaporation and energy budget in Lake Vegoritis, Greece. *J Hydrol* 345(3):212-  
757 223
- 758 Henderson-Sellers B (1986) Calculating the surface energy balance for lake and reservoir modeling: a review. *Rev Geophys*  
759 24(3):625-649
- 760 Jensen ME, Allen RG (1990) *Evapotranspiration and irrigation water requirements*. New York, ASCE Manuals and Reports  
761 on Engineering Practice 70
- 762 Jensen ME, Allen RG (2016) *Evaporation, evapotranspiration, and irrigation water requirements*. 2<sup>nd</sup> ed. Reston, ASCE  
763 Manuals and Report on Engineering Practice 70
- 764 Jin Z, Charlock TP, Smith Jr WL, Rutledge K (2004) A parameterization of ocean surface albedo. *Geophys Res Lett*  
765 31(L22301):1-4
- 766 Katsaros KB, McMurdie LA, Lind RL, Devault JE (1985) Albedo of a water surface, spectral variation, effects of  
767 atmospheric transmittance, sun angle and wind speed. *J Geophys Res* 90(C4):7313-7321
- 768 Kipp & Zonen (2010) CNR4 net radiometer instruction manual, version 1409. <http://kipzonen.com>. Accessed 23  
769 September 2015
- 770 Konda M, Imasato N, Nishi K, Toda T (1994) Measurement of the sea surface emissivity. *J Oceanogr* 50(1):17-30
- 771 Kohsiek W, Liebethal C, Foken T, Vogt R, Oncley SP, Bernhofer C, DeBruin HAR (2007) The Energy Balance Experiment  
772 EBEX-2000. Part III: Behaviour and quality of the radiation measurements. *Boundary-Layer Meteorol* 123(00):55-  
773 75
- 774 Kustas WP, Prueger JH, Hipps LE, Hatfield JL, Meek D (1998) Inconsistencies in net radiation estimates from use of  
775 several models of instruments in a desert environment. *Agric For Meteorol* 90(00):257-263
- 776 Kjaersgaard JH, Cuenca RH, Plauborg FL, Hansen S (2007) Long-term comparisons of net radiation calculation schemes.  
777 *Boundary-Layer Meteorol* 123:417-431
- 778 Kofronova J, Miroslav T, Sipek V (2019) The influence of observed and modelled net longwave radiation on the rate of  
779 estimated potential evapotranspiration. *J Hydrol Hydromech* 67(3):280-288
- 780 Li CW, Barnes IW (1980) The relationship between net and global radiation over water. *Theor Appl Climatol* 28(1):91-  
781 100
- 782 Liu H, Feng J, Sun J, Wang L, Xu (2015) An eddy covariance measurements of water vapor and CO<sub>2</sub> fluxes above the  
783 Erhai Lake. *Sci China Earth Sci* 58(3):317-328
- 784 Marquis P (2005) Turbidity and suspended sediment as measures of water quality. *Streamline Watershed Management*  
785 Bulletin 9(1):21-23
- 786 Monteith JL, Unsworth MH (2013) *Principles of environmental physics*. Academic Press, New York
- 787 Munro DS (2005) Boundary layer climatology. In: Oliver JE (ed) *Encyclopedia of world climatology*. Springer, Dordrecht,  
788 pp. 168-178
- 789 Myeni L, Moeletsi ME, Clulow AD (2020) Assessment of three models for estimating daily net radiation in southern  
790 Africa. *Agric Water Manag* 229(2020):105951
- 791 Nunez M, Davies JA, Robinson PJ (1972) Surface albedo at a tower site in Lake Ontario. *Boundary-Layer Meteorol*  
792 3(1):77-86
- 793 Oke TR (1995) *Boundary layer climates*. London, Routledge

- 794 Pashiardis S, Kalogirou SA, Pelengaris A (2017) Characteristics of longwave radiation through the statistical analysis of  
795 downward and upward longwave radiation and inter-comparison of two sites in Cyprus. *J Atmos Sol-Terr Phy*  
796 164(00):60-80
- 797 Payne RE (1972) Albedo of the sea-surf ace. *J Atmos Sci* 29(00):959-970
- 798 R Core Team (2017). R: A language and environment for statistical computing. R Foundation for Statistical Computing,  
799 Vienna, Austria. URL <https://www.R-project.org/>
- 800 Sauer TJ, Singer JW, Prueger JH, DeSutter TM, Hatfield JL (2007) Radiation balance and evaporation partitioning in a  
801 narrow-row soybean canopy. *Agric For Meteorol* 145(00):2016-214
- 802 Sene KJ, Gash JHC, McNeil DD (1991) Evaporation from a tropical lake: comparison of theory with direct measurements.  
803 *J Hydrol* 127(00):193-217
- 804 Shuttleworth WJ (2012) *Terrestrial hydrometeorology*. Wiley-Blackwell, Chichester
- 805 Vitale AJ, Genchi SA, Piccolo MC (2019) Assessing the surface radiation balance and associated components in an  
806 intertidal wetland. *J Coast Res* 35(1):158-164
- 807 Wozniak B, Dera J (2007) *Light absorption in sea water*. Springer, New York
- 808 Wright JL (1982) New evapotranspiration crop coefficients. *J Irrig Drain Eng* 108(IR2):57-74
- 809

# Figures

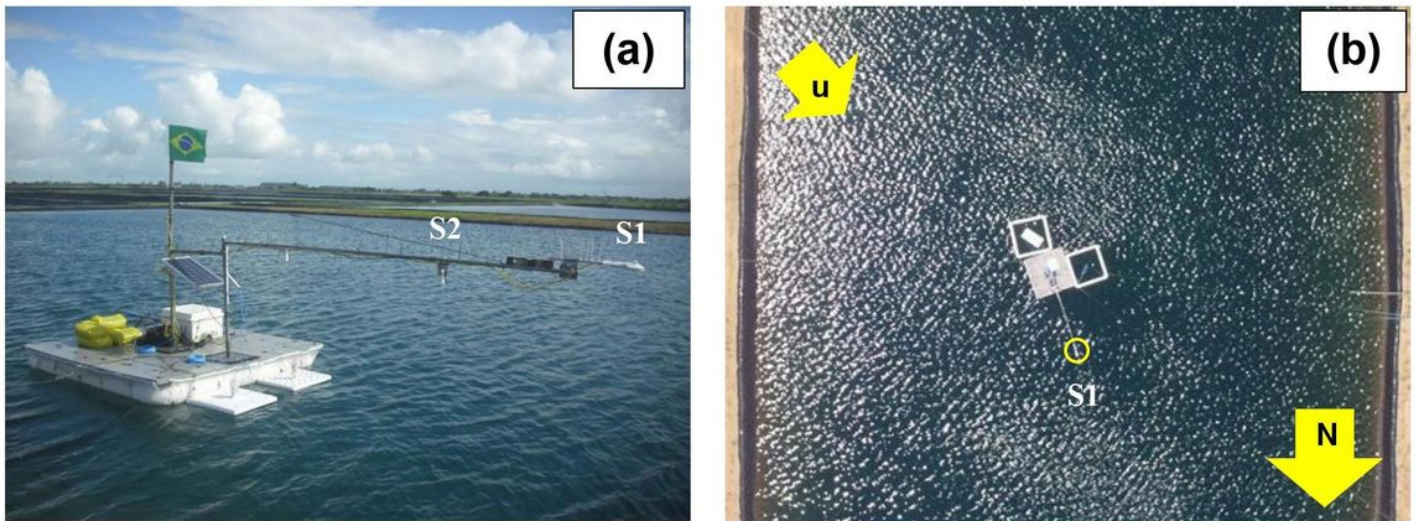


Figure 1

a, b The raft or floating platform (FP) over water with a four-component net radiometer (S1) and an infrared thermometer (S2) in the 2015 and 2016 campaigns. (u = predominant wind direction)

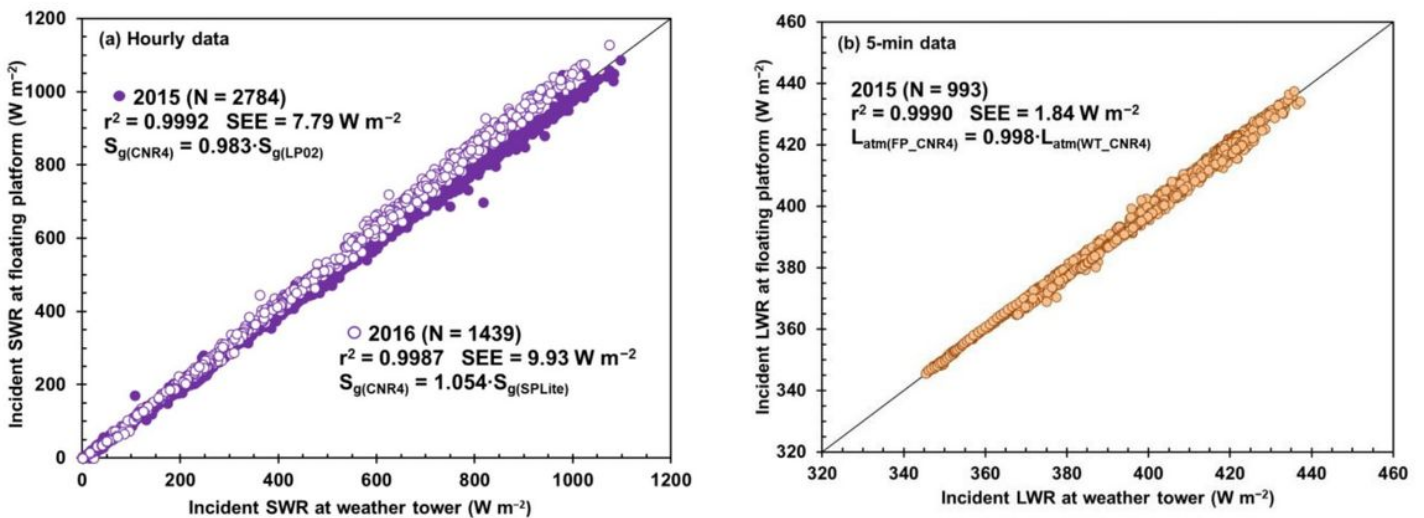


Figure 2

a, b Correlation between measurements of SW and LW radiation fluxes from the tripod-mounted weather tower and the floating platform. SW radiation was measured with pyranometers in the tower and with the CNR4 net radiometer in the floating platform while LW radiation was measured with two CNR4's. Data of (b) are from Borges et al. (2016)

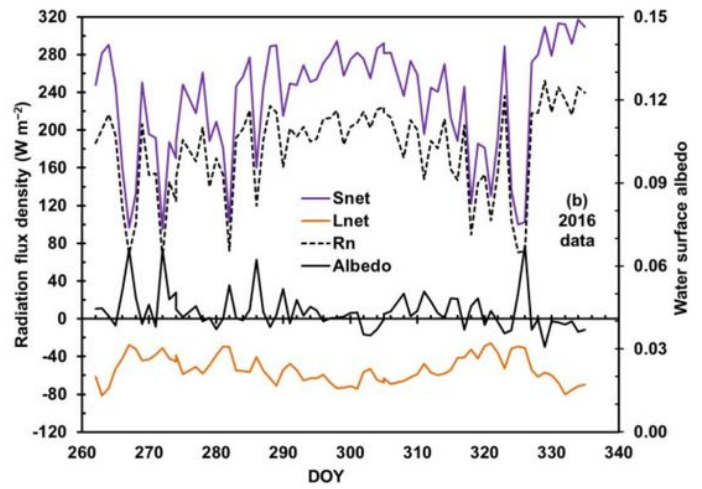
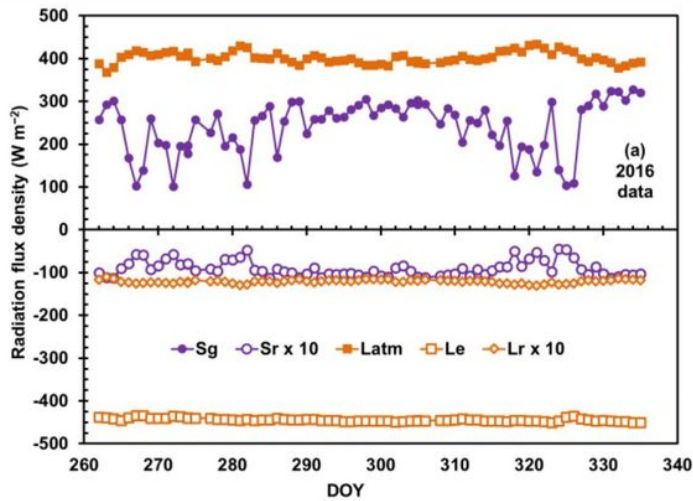


Figure 3

a, b Seasonal variation of daily components of the radiation balance over the surface of the low-turbidity water from 18th Sept. (DOY 262) to 30th Nov. 2016 (DOY 335)

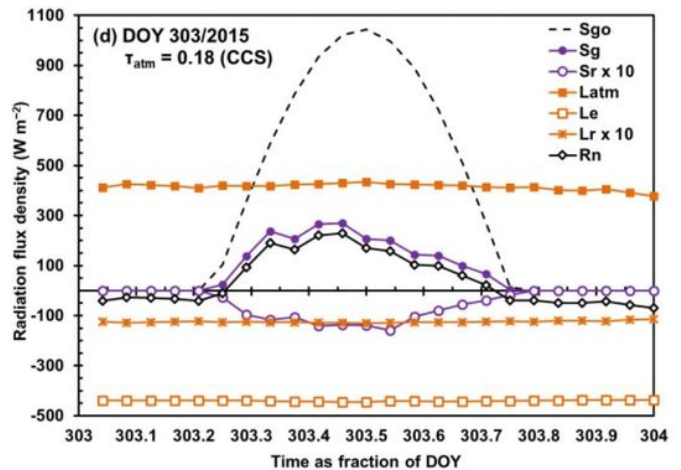
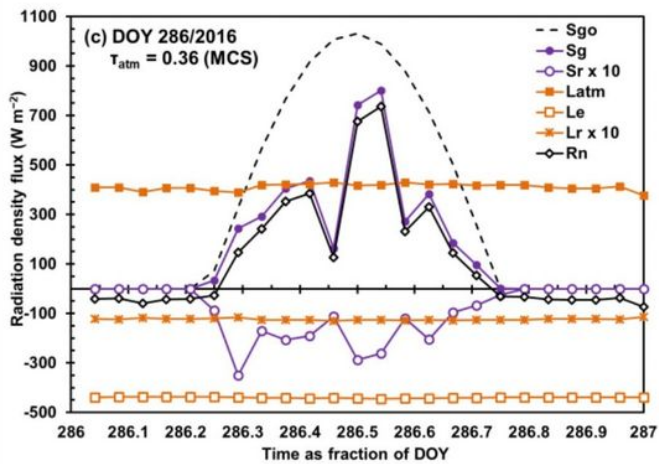
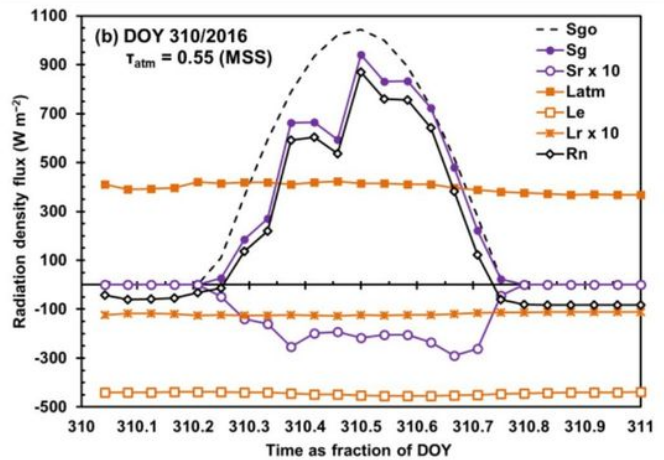
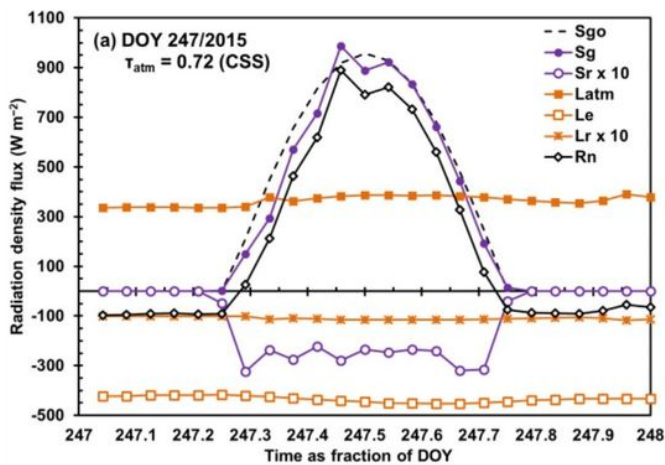


Figure 4

a, b, c, d Daily course of radiation balance components on the surface of low turbidity water as a function of cloud cover expressed by  $\tau_{atm}$  (the daytime atmospheric transmissivity) for the four selected days from 2015 and 2016. CSS = completely sunny (clear) sky, MSS = mostly sunny sky, MCS = mostly cloudy sky, and CCS = completely cloudy (overcast) sky

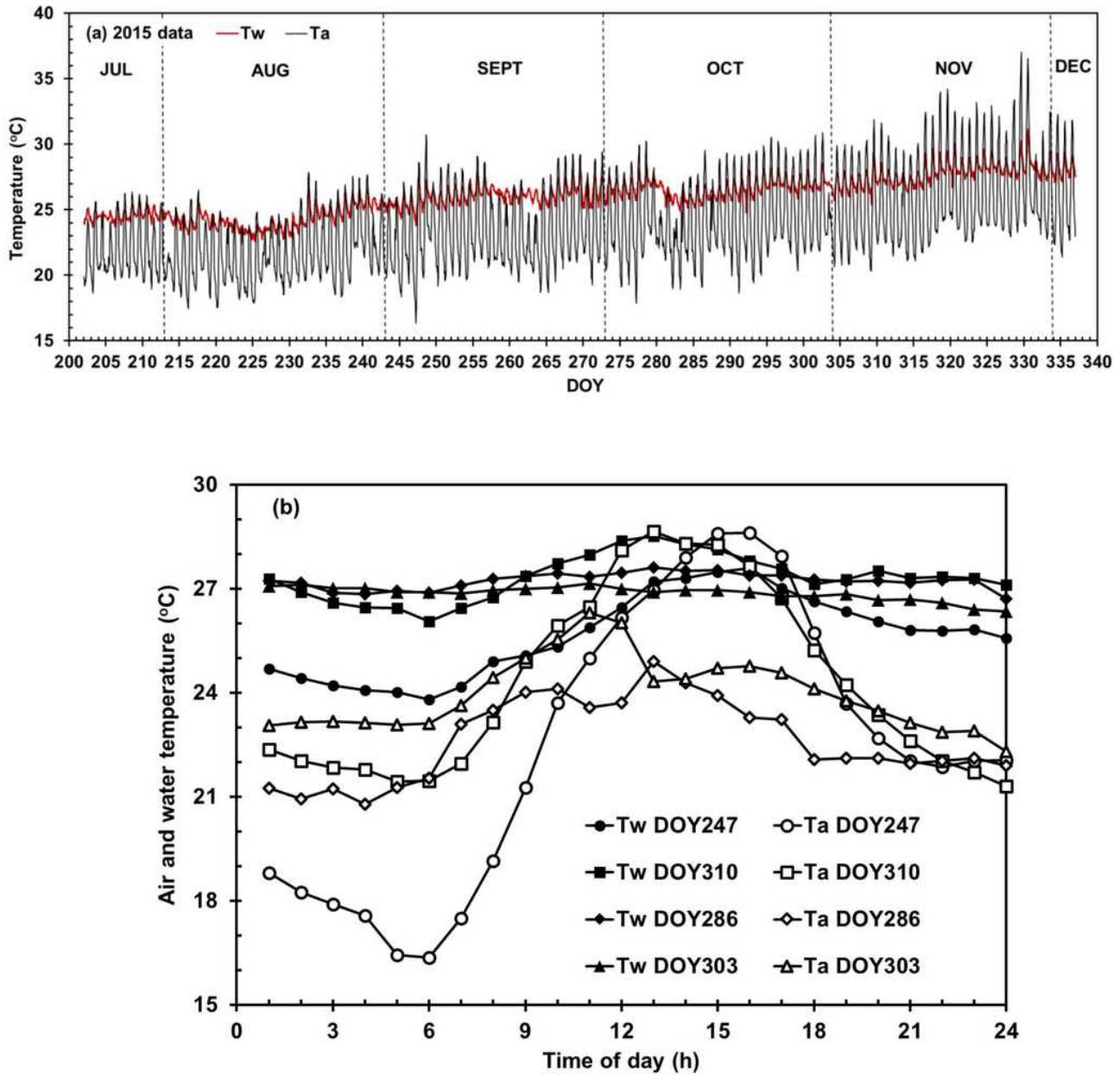


Figure 5

a, b Time trends in water surface (Tw) and air (Ta) temperatures from mid-July to early December 2015 and Tw and air temperature Ta for the selected days with contrasting cloud cover. DOY 247/2015 (CSS,  $\tau_{atm} = 0.72$ ), DOY 310/2016 (MSS,  $\tau_{atm} = 0.55$ ), DOY 286/2016 (MCS,  $\tau_{atm} = 0.36$ ), and DOY 303/2015

(CCS,  $\tau_{atm} = 0.18$ ). CSS = completely sunny (clear) sky, MSS = mostly sunny sky, MCS = mostly cloudy sky, and CCS = completely cloudy (overcast) sky

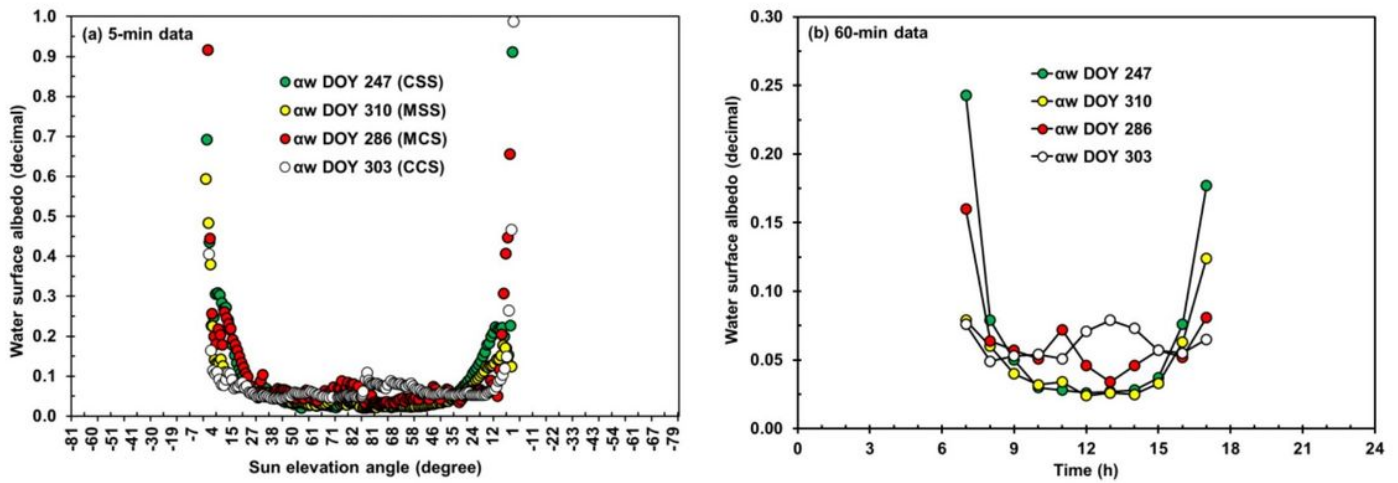


Figure 6

a, b Daily course of the low-turbidity water albedo  $aw$  for the four selected days with contrasting cloud cover. DOY 247/2015 (CSS,  $\tau_{atm} = 0.72$ ), DOY 310/2016 (MSS,  $\tau_{atm} = 0.55$ ), DOY 286/2016 (MCS,  $\tau_{atm} = 0.36$ ), and DOY 303/2015 (CCS,  $\tau_{atm} = 0.18$ ). CSS = completely sunny (clear) sky, MSS = mostly sunny sky, MCS = mostly cloudy sky, and CCS = completely cloudy (overcast) sky

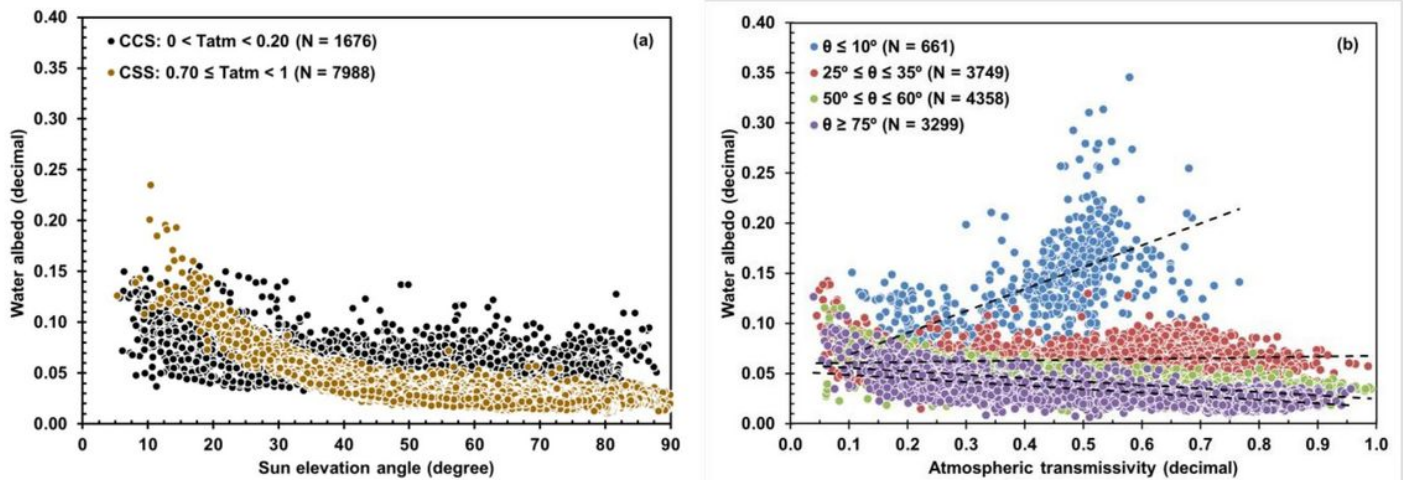


Figure 7

a, b Plot of low-turbidity water albedo against sun elevation angle for the two extreme conditions of cloud cover and against atmospheric transmissivity for SW radiation for four intervals of sun elevation angle

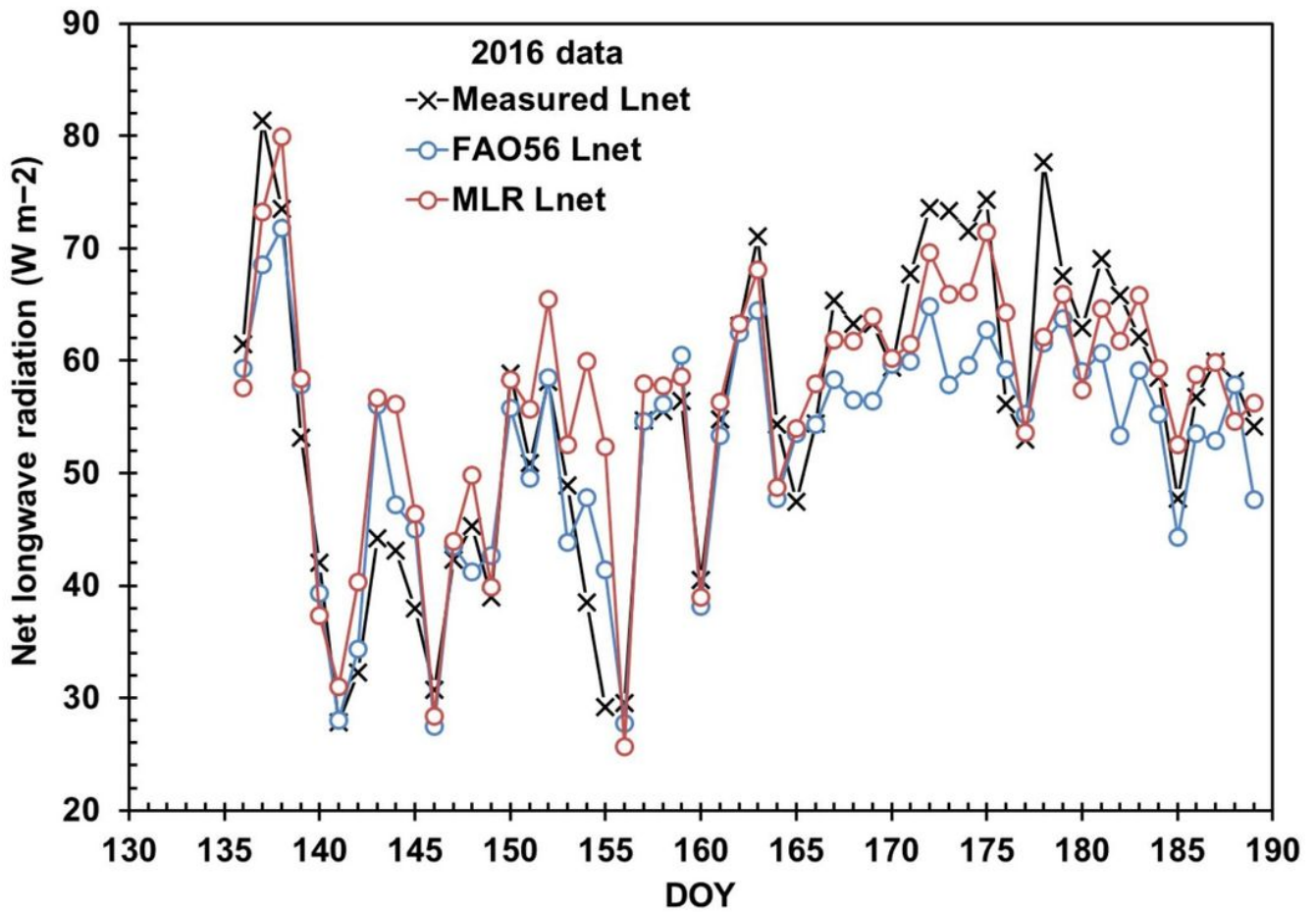


Figure 8

Course of measured and estimated daily net longwave radiation over the low-turbidity water surface in 2016 from DOY 136 to DOY 189 (54-day interval).

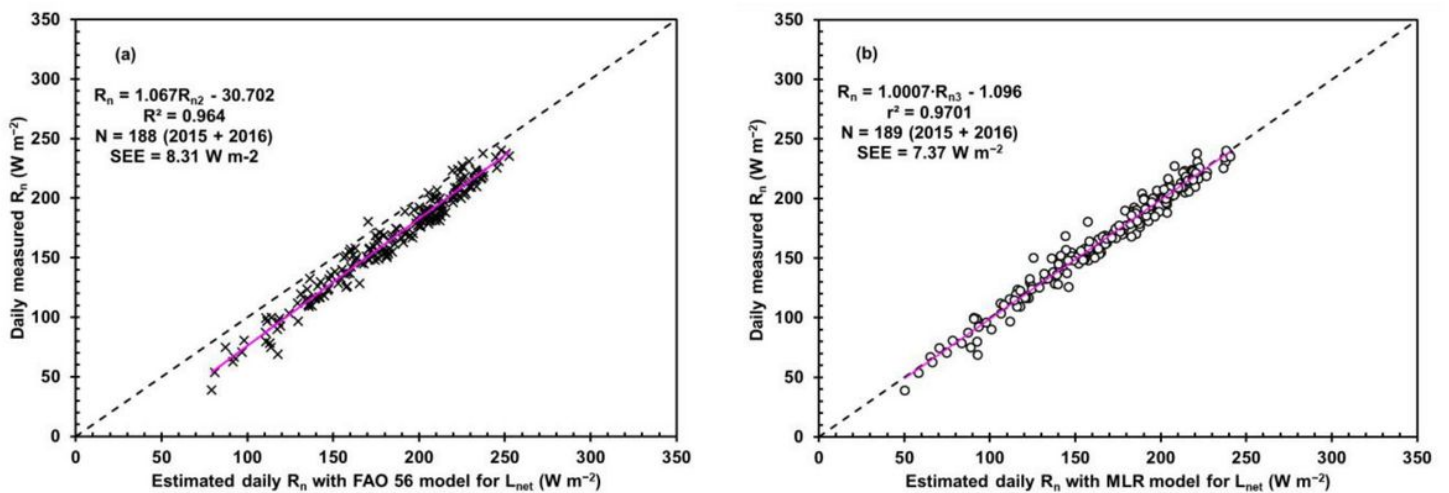


Figure 9

a, b Measured all-wave net radiation against calculated net-all wave radiation with Lnet(56) (a) and as Lnet(MLR), where 56 stands for FAO 56 Penman-Monteith equation and MLR stands for multiple linear regression model